

C.3

CIC-14 REPORT COLLECTION
REPRODUCTION
COPY

*Comparison of the Fork and Python
Spent-Fuel Detectors*



Los Alamos

*Los Alamos National Laboratory is operated by the University of California for
the United States Department of Energy under contract W-7405-ENG-36.*

*Edited by Paul Henriksen, Group IS-11
Prepared by Jo Ann Barnes, Group N-1*

An Affirmative Action/Equal Opportunity Employer

This report was prepared as an account of work sponsored by an agency of the United States Government. Neither the United States Government nor any agency thereof, nor any of their employees, makes any warranty, express or implied, or assumes any legal liability or responsibility for the accuracy, completeness, or usefulness of any information, apparatus, product, or process disclosed, or represents that its use would not infringe privately owned rights. Reference herein to any specific commercial product, process, or service by trade name, trademark, manufacturer, or otherwise, does not necessarily constitute or imply its endorsement, recommendation, or favoring by the United States Government or any agency thereof. The views and opinions of authors expressed herein do not necessarily state or reflect those of the United States Government or any agency thereof.

*Comparison of the Fork and Python
Spent-Fuel Detectors*

P. M. Rinard

*G. Bignan**

*J. Capsie**

*J. Romeyer-Dherbey**



**Centres d'Etudes Nucleaires de Cadarache, Service Systems d'Aides a l'Exploitation,
13115 Saint Paul Lez Durance Cedex FRANCE*

CONTENTS

ABSTRACT.....	1
I. INTRODUCTION	2
II. THE EQUIPMENT	3
A. Fork Detector.....	3
B. PYTHON Detector.....	6
C. COBRA Tank and Assemblies	8
III. FORK MEASUREMENTS.....	10
A. Neutron Measurements.....	10
1. Standard Assembly	10
a. Boron Effects	11
b. Gadolinium Effects.....	11
2. Small Assembly and Multiplication Effects.....	12
B. Gamma-Ray Measurements.....	12
1. Source Position Sensitivity.....	12
2. Scattering by Neighboring Pins.....	13
IV. PYTHON MEASUREMENTS	45
A. Neutron Measurements.....	45
1. Standard Assembly.....	45
a. Boron Effects	45
b. Gadolinium Poison Effects	45
2. Small Assembly and Multiplication Effects.....	45
B. Gamma-Ray Measurements.....	46
V. FORK AND PYTHON COMPARISONS.....	62
A. Neutron Measurements.....	62

CONTENTS (cont)

1. Standard Assembly.....	62
a. Source Position Sensitivities.....	62
b. Total Count Rates	63
c. Gadolinium Poison Effects	64
2. Small Assembly and Multiplication Effects.....	64
B. Gamma-Ray Measurements: Source Position Sensitivities.....	64
C. Correlation Summary.....	64
1. Neutrons.....	64
2. Gamma Rays.....	65
VI. SUMMARY.....	65
A. Objectives and Instrument Features.....	65
B. Responses and Correlation.....	70
VII. ACKNOWLEDGMENTS.....	70
REFERENCES	71

COMPARISON OF THE FORK AND PYTHON SPENT-FUEL DETECTORS

by

P. M. Rinard, G. Bignan, J. Capsie, J. Romeyer-Dherbey

ABSTRACT

Instruments to measure radiations from spent-fuel assemblies have been developed in the United States and in France. They have different objectives (safeguards and criticality safety) that have led to different designs, but are nevertheless sufficiently similar to compare and correlate.

Small capsules of ^{252}Cf and ^{137}Cs were placed in a fuel pin and moved through a 17 x 17 array of pins. By raising the source pin, axial profiles were measured to help determine the total responses of the instruments to complete assemblies. The measurements show the relative contributions to the detectors' responses of neutrons and gamma rays from different pin locations. Sums of these measurements simulate total responses and how the instruments are correlated. Neutron absorbing pins containing gadolinium were inserted into the assembly to measure the dampening of the neutron count rates. These results will be useful in understanding the responses of spent fuel and fresh mixed-oxide fuel stored underwater with poison rods.

I. INTRODUCTION

Nondestructive measurements to characterize spent-fuel assemblies stored underwater can serve safeguards and plant safety purposes. The two spent-fuel detectors discussed in this report have been developed in the United States at Los Alamos National Laboratory (LANL) and in France at the Cadarache Center for Nuclear Studies (Cadarache). As part of a bilateral agreement, the two countries exchanged information about the detectors and jointly measured fuel assemblies with the detectors to further characterize, compare, and correlate them.

The LANL fork and the Cadarache PYTHON detectors have much in common, but also have significant differences because they were designed for different purposes.

- (1) The fork was developed for the International Atomic Energy Agency (IAEA) to safeguard spent fuel in storage ponds and it has been used by the IAEA and EURATOM for that purpose. The concern addressed by the PYTHON detector is the avoidance of a criticality accident while handling and transporting spent-fuel assemblies from a power plant to a reprocessing plant; this is part of the French national nuclear power program.
- (2) The fork is designed for portability and rapid measurements. It can be assembled and attached to the bridge of a spent-fuel pond in about 30 min. The fork is placed around an assembly that is partially raised from its storage rack. PYTHON normally remains on a pond's rack for an extended period of time and assemblies are brought to it. The large size and weight of PYTHON is no hindrance because it is only rarely moved.
- (3) The data analyses of both detector systems are to verify the operator-declared exposures and cooling times.
- (4) Both detectors use fission chambers for neutron counting and ionization chambers for gross gamma-ray measurements. Each detector places fission and ionization chambers on opposite sides of an assembly. The fork has a set of fission chambers surrounded by cadmium-covered polyethylene and another set without this barrier to thermal neutrons. PYTHON has fission chambers surrounded by polyethylene wrapped in both cadmium and boron carbide; hence both thermal and epithermal neutrons are excluded from the detector.
- (5) Each fission chamber in PYTHON has 800 mg of ^{235}U , compared with only 132 mg in a fork's fission chamber, but PYTHON neutron count rates are

about 20% of the fork's count rates because the PYTHON fission chambers are farther from the assembly.

- (6) Active neutron interrogation may be done with PYTHON by alternately placing a ^{252}Cf source near one side of the assembly and removing it while slowly moving the assembly through the detector. The cadmium and boron carbide wrappings around the fission chambers, along with the water-filled gap between the assembly and the detector, reduce the background rate from ^{252}Cf neutrons during active interrogation.

Additional comparisons will be made throughout this report. Each detector and its measured responses will be described before being compared and correlated.

II. THE EQUIPMENT

A. Fork Detector

The fork detector has been described in previous reports^{1,2} and its measurement characteristics studied.^{2,3} Only a brief overview of the detector will be presented here.

The detector head has a polyethylene body in the shape of a fork with two tines. Each tine holds a fission chamber surrounded by cadmium-wrapped polyethylene to detect neutrons with greater than thermal energies, another fission chamber without a cadmium wrap that is sensitive to thermal neutrons, and an ionization chamber that responds to gamma rays of all energies. The tines are placed on opposite sides of an assembly; it has been found^{1,4} that measurements from additional sides are unnecessary.

The cadmium-wrapped and bare fission chambers provide the IAEA with a means of determining the concentration of boron in a pond's water independently of the reactor operator. The concentration strongly affects the neutron signal³ and to compare data among various ponds the data must be normalized to a selected concentration. This indirect method of measuring the concentration is provided because of the lack of a portable, rugged chemical instrument.

The fission and ionization chambers have active lengths of 6 in. (15.24 cm). Each fission chamber has 132 mg of ^{235}U . The ionization chambers are filled with air at 1 atm pressure. A fork detector head is shown in Fig. 1 along with a GRAND-I electronics unit (D. S. Davidson and Co.) and a representative portable computer. Not shown are pipes that connect the detector head to the fuel pond's bridge. In addition to

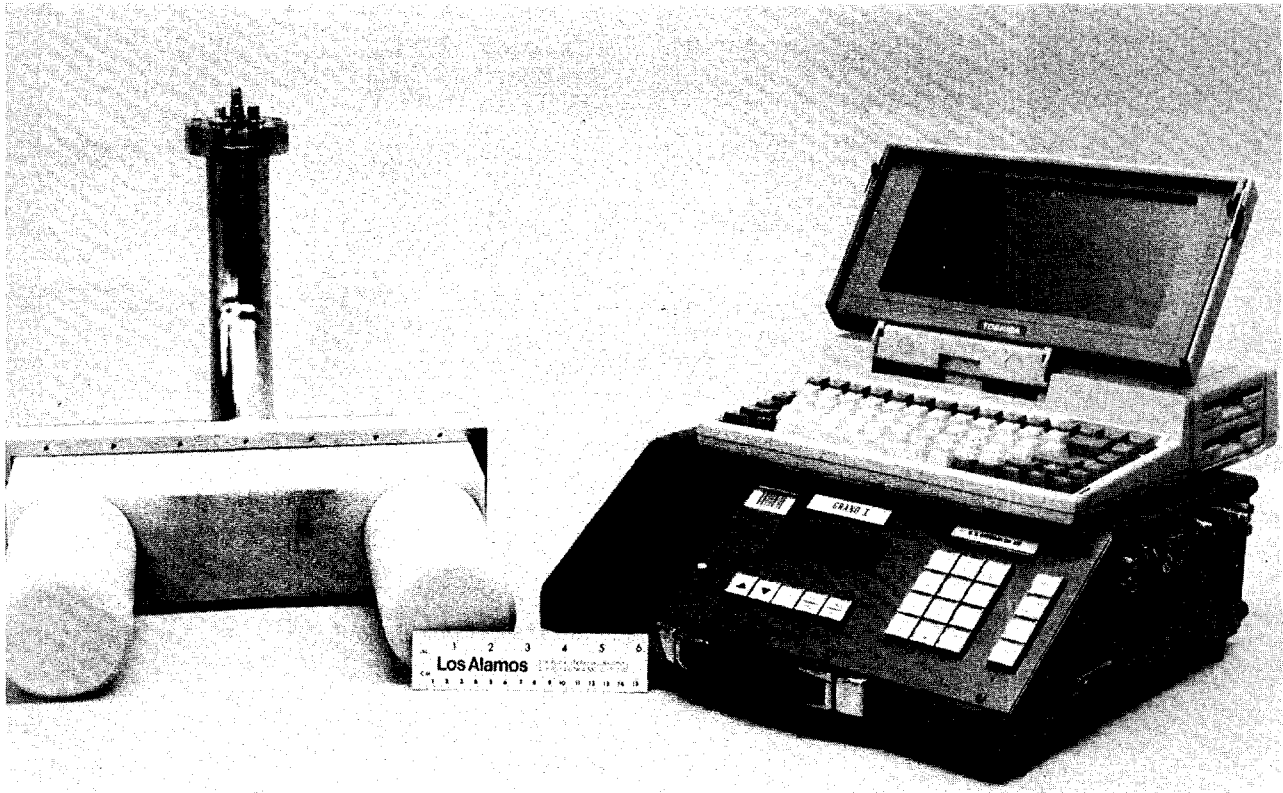


Fig. 1. The fork detector head is on the left of this photograph. It is constructed from polyethylene and contains fission chambers and ionization chambers in each tine. Preamplifiers for the fission chamber pulses are inside the stainless-steel pipe attached to the rear. Additional pipes (not shown) are used to position the fork and pass electrical cables to the surface. The Davidson GRAND-I electronics unit is on the right beneath a representative portable computer.

supporting and positioning the fork, the pipes form a conduit for the electrical wires between the detectors and the GRAND-I and contain preamplifiers for the fission chamber pulses. Figure 2 indicates how these sections of the detector system are arranged at a pond.

The GRAND-I electronics unit provides the high and low voltages and processes the pulse (neutron) and current (gamma-ray) signals while operating entirely on internal batteries. The small GRAND-I enhances the portability of the fork detector; its battery operation is a great convenience on a pond's bridge as well as an electrical safety feature.

A portable computer may be attached to the GRAND-I during data acquisition, but it is not required. The GRAND-I has a small printer for data logging and can hold the data for one day in its memory; the data can be transferred to a computer's memory at a later time.

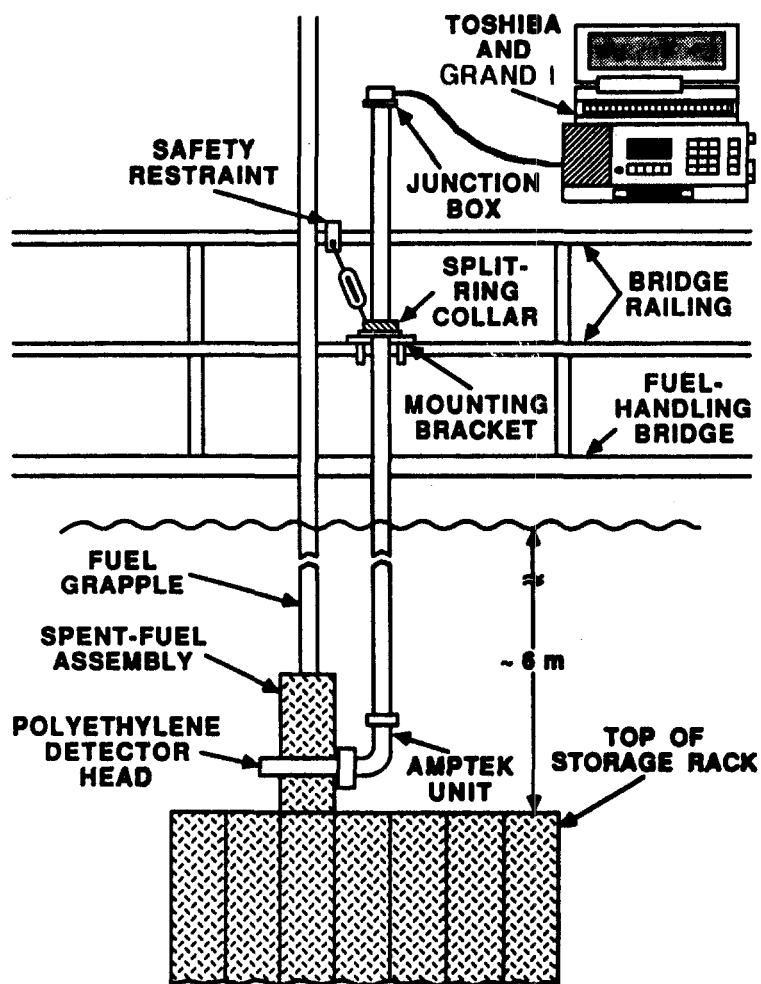


Fig. 2. This is a schematic drawing of the fork at a spent-fuel pond. The GRAND-I and computer are on the pond's bridge. The fork detector head is around a partially raised assembly. Pipes between the detector head and the GRAND-I carry the electrical cables. The mounting bracket, split-ring collar, and safety restraint transfer the weight of the fork to the rail. A user only needs to hold the fork against the assembly.

However, the advantage of using a computer during the collection of the data is that a complex but nearly instantaneous analysis of the data will be made and irregular data brought to the user's attention even before removing the fork from an assembly.⁵ The measurement can be repeated to determine if the first data were in error; if the irregular data are replicated, further measurements may be made at other positions along the length of the assembly. Without the rapid analysis of the computer on the bridge, an anomaly may not be apparent until days later when it is impossible to investigate the assembly further.

A fork detector can be shipped to a storage pond in three boxes and assembled in about 30 min. The detector head is easily positioned by one operator while a second controls the GRAND-I (and the computer, if one is used). The neutron count rates are large enough to gather 10 000 to 30 000 counts in 30 to 60 s; the gross gamma-ray currents are determined in only a few seconds. Time is also needed to lower the

assembly into the rack, move the bridge to another assembly and partially raise the new assembly. The total time required for a single assembly has varied from 5 to 9 min, depending on the circumstances at the pond.

Consistency among the operator's declared exposures and cooling times can be determined from the data; the sensitivity of the fork to diversions of fuel and misdeclarations has been analyzed elsewhere.²

B. PYTHON Detector

PYTHON has a detector head in two sections, a set of NIM electronics, and a ^{252}Cf source if active neutron interrogation is to be used. A sketch of the equipment is shown in Fig. 3.

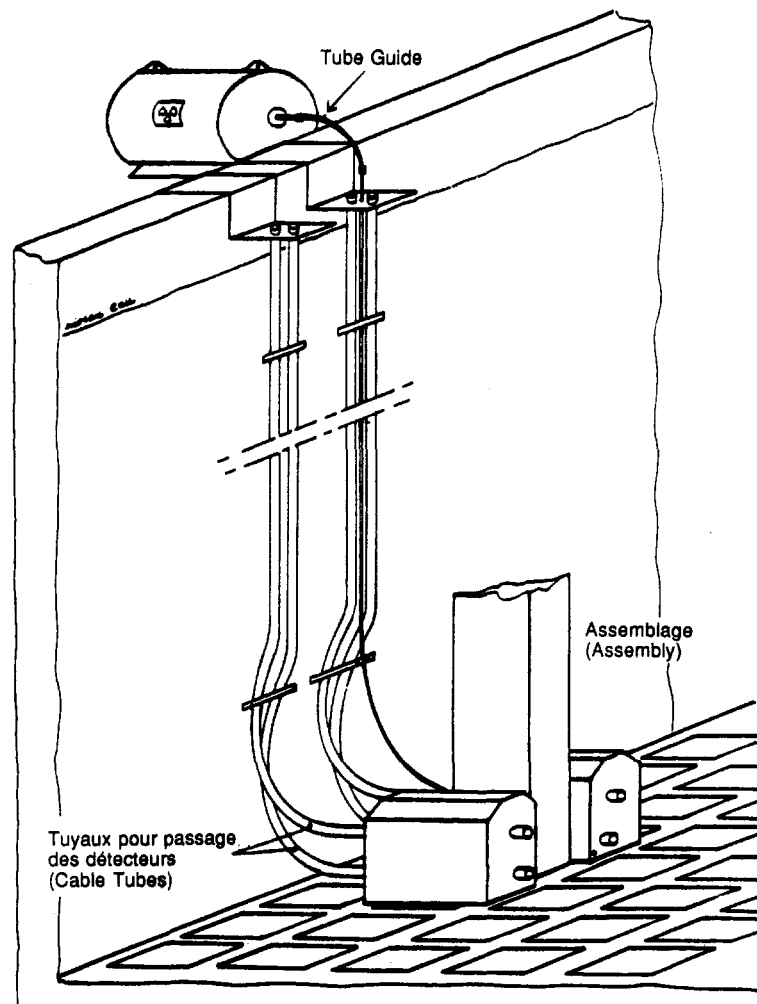


Fig. 3. The PYTHON detector has two sections resting on the storage rack and assemblies pass between them. Pipes contain the electrical cables that link the detector heads with NIM electronics on the surface. A ^{252}Cf source can be pneumatically driven between its storage housing at the side of the pond and a location beside an assembly. This figure is from Ref. 7.

The two sections of the detector head are partially inserted into a pond's rack with an empty storage location between them. An assembly can be raised or lowered between the two sections. As shown in Fig. 4, the fission chamber in a section is inside polyethylene wrapped in cadmium and boron carbide (to eliminate thermal and epithermal neutrons). The ionization chamber is encased in lead with a collimator slit facing the assembly. Pipes route cables between the detector head and the electronics near the pond.

If active neutron interrogation is to be performed, a ^{252}Cf source is pneumatically driven between a shielded container at the pond's edge and a position between the assembly and one section of the detector head. An assembly continuously moves through the sections and many passive and active measurements are made (Fig. 5) with the fission chamber in the section across the assembly from the source.⁶ The geometry of PYTHON was optimized for the active interrogation so that the neutrons coming directly from the ^{252}Cf source into the detector would have a relatively small effect.

Each fission chamber has 800 mg of ^{235}U in a vertical plate; the active length is 22 cm. The ionization chambers are filled with air at 1 atm pressure and have an active length of 12 cm.

PYTHON is not designed to be a portable instrument so the electronics consist of standard NIMs in a bin near the pond's edge. The fission chambers' pulses are

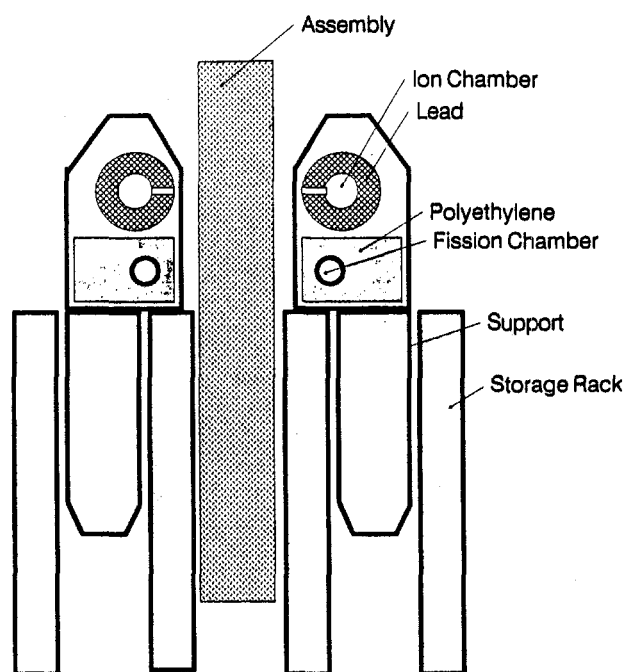


Fig. 4. This side view of the PYTHON detector head shows the supports that fit into the storage rack and the detectors themselves. The upper detector in each section is an ionization chamber surrounded by a lead collimator. The lower detector is a fission chamber within polyethylene wrapped in cadmium and boron carbide.

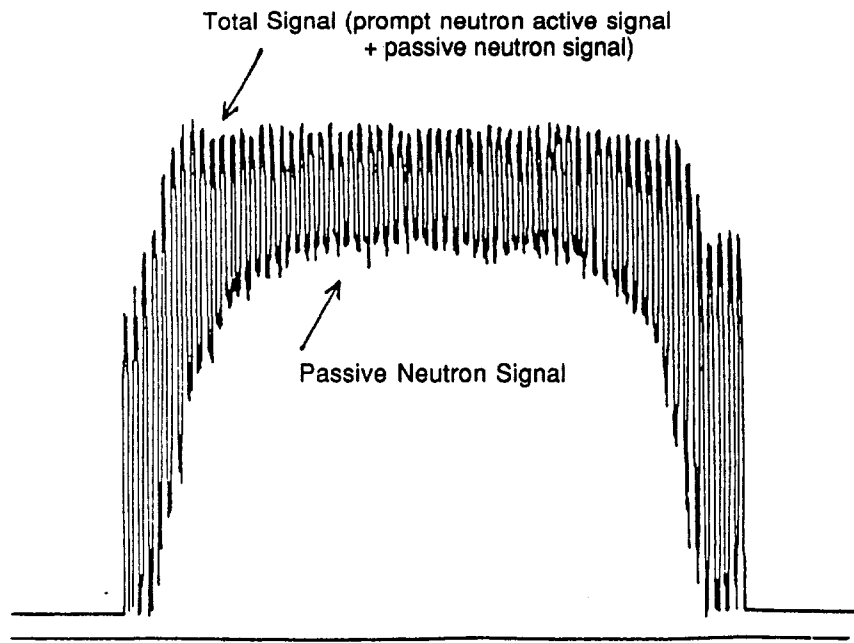


Fig. 5. If an assembly passes through the detector head and the ^{252}Cf source is periodically driven near the assembly and then returned to its storage housing, both passive and active neutron counts are taken alternatively. The passive signal is the lower envelope of the curve in this figure; the active signal is the difference between the upper and lower envelopes. This figure is from Ref. 6.

converted to TTL signals and counted by a multichannel scaler in a computer. The ionization chamber currents are converted to frequencies and also measured in the computer.

C. COBRA Tank and Assemblies

Measurements were made with the fork and PYTHON detectors at Cadarache in a water-filled tank called COBRA (Fig. 6) constructed for instrument development purposes. One side of the tank can hold a simulated assembly and detector. The other side has a shielded ^{252}Cf source that can be driven near the assembly; this feature of COBRA was not used during these measurements.

It was impractical to measure spent-fuel assemblies, so we measured fresh fuel assemblies. Californium-252 and ^{137}Cs sources were placed in the middle of a pin, which was moved throughout the array of pins in the assembly. The signals generated by a spent-fuel assembly (although with an unusually high multiplication) could be simulated in this manner with the advantage of learning the relative importances of

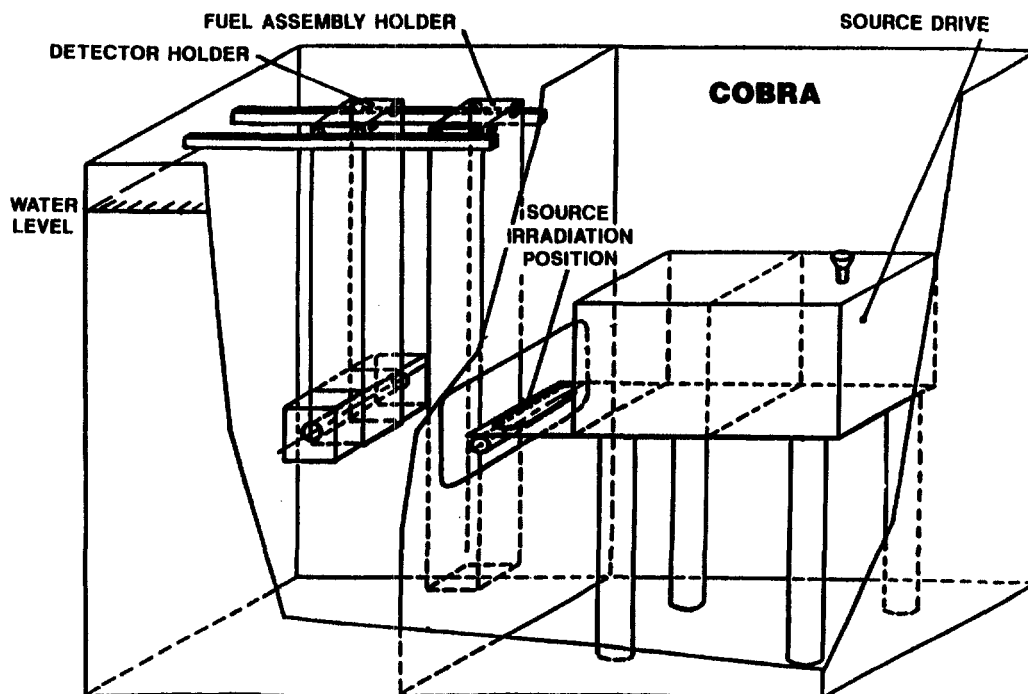


Fig. 6. The measurements were made in this water-filled tank called COBRA. The assemblies and detectors were placed in the left side of the tank. The right side is designed to hold a ^{252}Cf source which can be moved to an irradiating position adjacent to an assembly for active interrogation studies; this feature of the tank was not used. This sketch shows a prototype detector in a holder. For the present measurements, the fork detector hung from a special bracket and PYTHON was supported from the floor of COBRA; thus the detector holder was not used. This figure is from Ref. 7.

radiations emitted from individual pins. The ^{252}Cf source emitted 9.5×10^5 n/s and the ^{137}Cs source had a strength of 32.2 mCi (1.19×10^9 gammas per second).

The standard assembly was a pressurized-water reactor (PWR) 17×17 array of pins with 3.5% ^{235}U enrichment. The pitch of the array was 1.26 cm. The pellets used in the pins had diameters of 7.2 mm. The wall thickness of the aluminum cladding was 1.05 mm. The height of each pin was 80 cm.

To study the effect of poison rods, additional pins with gadolinium were inserted in water channels inside the array. Pins with depleted uranium (0.25% ^{235}U) were also used in a smaller 9×9 array.

Spent-fuel assemblies are often stored in water containing dissolved boron. To simulate this condition, but to avoid the problems of adding boron to all the water in COBRA, a smaller tank was placed inside COBRA that would hold the assembly and detector. Boron was added to only this inner tank. The concentrations of boron were

not exactly the same for the two detectors, but the chemical analysis results in Table I show that the differences are slight and will be generally ignored here.

TABLE I. Boron Concentration (ppm)

Nominal	Fork Measurements	PYTHON Measurements
0	0	0
500	452	520
2000	2070	2170
3000	3060	2829

Values of k_{eff} for the 17 x 17 array at 0, 500, 1000, 2000, and 3000 ppm of boron have been calculated⁷ to be 0.806, 0.7136, 0.6507, 0.5768, and 0.525.

Neutron and gamma-ray backgrounds at the COBRA location were much smaller than the measurement uncertainties and could thus be ignored.

III. FORK MEASUREMENTS

A. Neutron Measurements

1. Standard Assembly. The standard assembly was a PWR 17 x 17 array with 3.5% ²³⁵U enrichment. The neutron or gamma-ray source was in one of the pins and in the plane of the fork's tines; this special pin was moved throughout the array to examine the sensitivity of the signals to the source location. The source pin could also be raised above this plane. We did not have time to use every pin location, so we selected a representative set of locations. The concentration of boron in the water could be varied and pins with gadolinium poison inserted into the assembly.

The source pin was placed in 37 locations throughout columns 1-9, as marked in Fig. 7. To check that such a sampling adequately represents the response from all pin locations, data taken previously³ at every pin location of a 15 x 15 array were examined. Data were used from 34 of the 204 locations, using a pattern similar to that of Fig. 7. The ratios of the sums of count rates from all 204 locations to the sums from 34 locations were calculated to be 6.123 ± 0.029 and 6.104 ± 0.026 for the cadmium-wrapped and

bare fission chambers, respectively; these ratios were computed at 0, 500, 1000, 2000, and 3000 ppm of boron in the water. With 204 being 6 times 34, it is concluded that the reduced set of pin locations can be used to characterize the response from all pins with no significant error (less than 0.5%).

a. **Boron Effects.** At boron concentrations of 0, 452, 1010, 2070, and 3060 ppm, the pin with the ^{252}Cf source was placed at the 37 locations. At four of those locations, the source pin was raised as much as 20 cm above the fork to measure the axial response profile. The neutron background was about 0.2 counts/s, which was negligible compared with the ^{252}Cf signals.

The data gathered with the ^{252}Cf in the plane of the fork's tines from the two sets of fission chambers are shown in Figs. 8-12; the data are shown at the array locations of the ^{252}Cf source. The same data are shown graphically in Figs. 13-20.

Data were taken with the ^{252}Cf raised above the plane of the fork's tines. These are given numerically in Tables II-VI and graphically in Figs. 21-22. Tables II-IX follow Fig. 34.

As the boron concentration increases, the depression of the count rates is clearly seen in the figures. The decreased sensitivity to pins away from the centers of the fission chambers is also apparent. The sums of counts at each concentration are given in Table VII and plotted in Fig. 23 for both the cadmium-wrapped and bare detectors. The count rates from columns 1-8 were doubled to simulate the unmeasured contributions from columns 10-17.

b. **Gadolinium Effects.** Poison pins are normally inserted into every water channel of an assembly, but in this case there were only enough pins with Gd_2O_3 to place in half the assembly (columns 3, 4, 6, and 9 of Fig. 7). The ^{252}Cf source was kept within that half of the assembly, so the effect of the missing poison pins should be small. No boron was present during these measurements with poison rods. The pins had 8% Gd_2O_3 by weight.

Poison pins with Gd_2O_3 are often used in PWR assemblies while inside the reactor core. Spent fuel assemblies in storage ponds generally have poison pins containing boron rather than gadolinium. Fresh mixed-oxide (MOX) assemblies, however, are stored under water with gadolinium poison pins. The data reported here are thus suggestive of the effects of boron pins in spent light-water reactor assemblies and of gadolinium pins in fresh MOX assemblies.

Data were taken only without boron in the water and are displayed in Fig. 24. Ratios of count rates in the cadmium-wrapped fission chambers with and without the

gadolinium pins are shown in Fig. 25. To a good approximation, the gadolinium pins affect the count rates from all other pins equally. This is not surprising considering that the purpose of the poison rods is to flatten the flux profile across an assembly.

2. Small Assembly and Multiplication Effects. Enough pins with depleted uranium (0.25% ^{235}U) were available to make a 9×9 array without water channels. Although this type of array is not used in fuel assemblies, the opportunity was taken to compare 9×9 arrays with depleted uranium and 3.5%-enriched uranium pins. These data can be used to check reactivity calculation codes for an unusual geometry.

The small array was placed adjacent to one tine of the fork, as shown in Fig. 26. Data were taken with the ^{252}Cf source along all of row H, the center row in this case. The only other data were from positions G-5 and I-5 and are essentially equal to that from H-5. All these data are shown in Figs. 27-29.

Normalized count rates from depleted and enriched pins are given in Figs. 30-31. As the ^{252}Cf source is moved farther from the tine the lack of multiplication within the array of depleted pins is apparent as the count rate decreases more rapidly than counts from pins with enriched fuel.

Monte Carlo calculations were performed with this array, and calculated k_{eff} values of 0.131 and 0.499 were obtained for the 9×9 arrays of depleted and enriched pins (with 1σ uncertainties of 0.002). For comparison, the k_{eff} value of the 17×17 array with 3.5%-enrichment pins was 0.806. The corresponding multiplications (the "net leakage multiplication" of Ref. 8) in the count rates of the 9×9 arrays are 1.09 and 1.59, respectively. The ratio of these multiplications is 0.686 while the ratio of the average count rates is 0.600 (for both cadmium-wrapped and bare fission chambers). These types of data serve as benchmarks for computer codes that must be used in more important situations where measurements have not been made.

B. Gamma-Ray Measurements

1. Source Position Sensitivity. Gamma rays from a pin will not be multiplied like neutrons, but they must penetrate water and other pins to reach the ionization chambers in a detector. Gamma rays of several different energies are important in spent-fuel studies^{9,10} but the most important is the 662-keV gamma ray from ^{137}Cs . A 32.2-mCi source of this isotope was placed in the center of one of the pins and moved through the array. The 17×17 array of enriched uranium pins was used, but the enrichment was unimportant.

The gamma-ray signal from the GRAND-I is proportional to the current in the ionization chambers. With this small source the signal was much weaker than with a spent-fuel assembly and showed fluctuations. We observed readings about 1 s apart and formed an average based on the range of values and the most commonly observed value. Signals from spent-fuel assemblies are about 1000 times larger and do not fluctuate.

With the ^{137}Cs source in the plane of the fork's tines, the data recorded are shown in Figs. 32-33. As the source moved toward the center of the assembly, the decrease in the GRAND-I reading was very nearly exponential, even when the row included a water channel or two instead of fuel pins. The coefficient of the exponential (the linear attenuation coefficient) varies with the row of pins, as given in Table VIII. The values of μ in Table VIII are between those for water (0.0856 cm^{-1}) and UO_2 (1.19 cm^{-1}) at 662 keV, as is reasonable.

Axial displacements of the ^{137}Cs source produced the profiles given in Fig. 34 and Table IX.

Based on calculations¹⁰ of the attenuation of gamma rays through an assembly and into air-filled collimator tubes, it has been assumed that gamma rays from only the first two or three columns could reach the ionization chambers in significant numbers. These measurements show that a few more columns should be considered for exacting work. These data also should be incorporated into studies of the type in Ref. 2.

2. Scattering by Neighboring Pins. A quick test was made to see if gamma rays from one pin are significantly scattered by neighboring pins into the fork. The ^{137}Cs source was placed in location I-1 (adjacent to the fork tines) and neighboring pins at locations I-2, H-1, and H-2 were individually removed. No change in the GRAND-I readings were seen.

This observation provides some justification for ignoring such scattering in simple gamma-ray transport calculations. More detailed Monte Carlo calculations include scattering effects automatically.

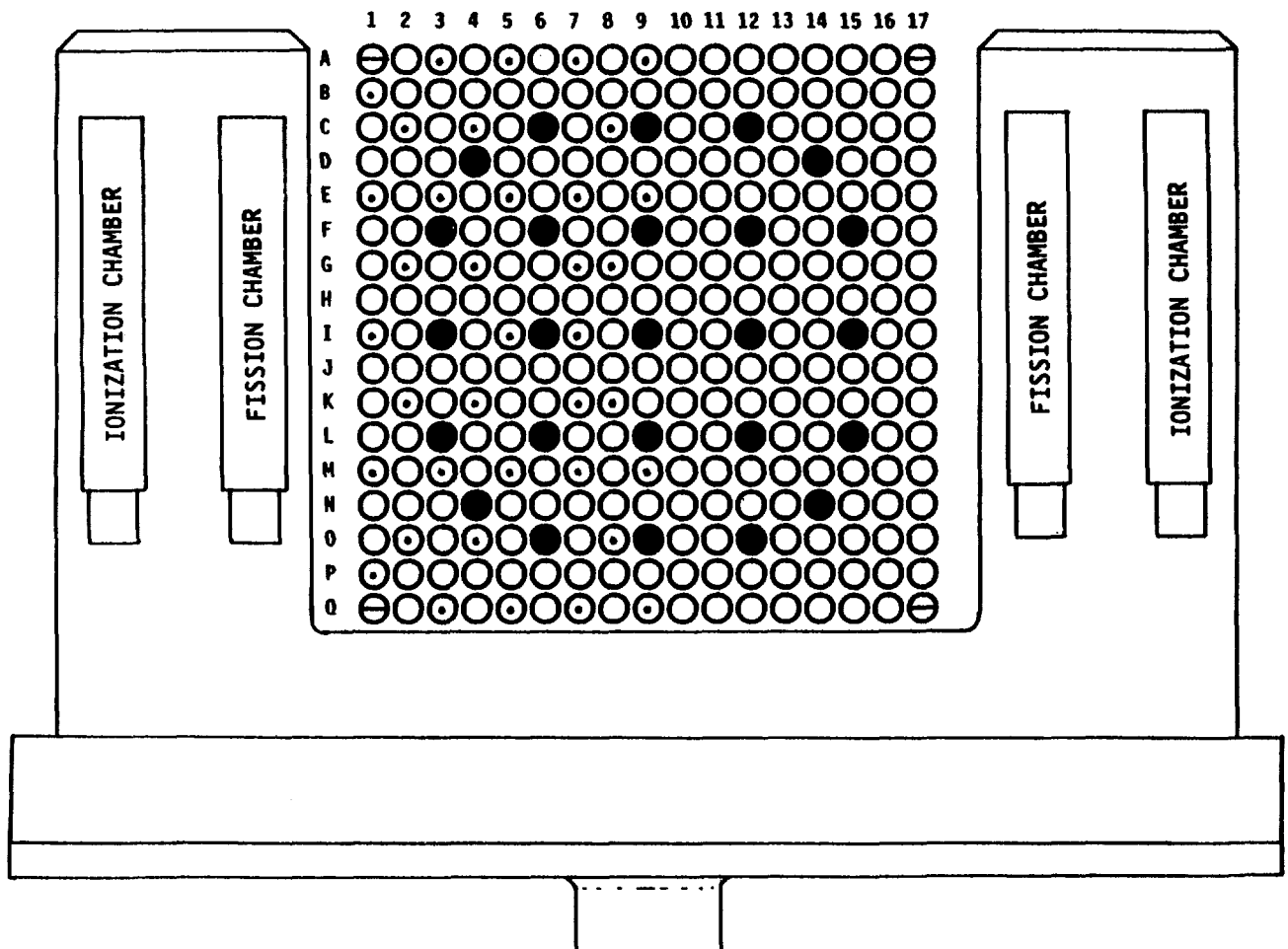


Fig. 7. The 17 x 17 array of PWR pins is surrounded by the fork detector and viewed from above the fork. The cadmium-wrapped and bare fission chambers are in the same vertical plane so only one is shown in this view. A diagram with the PYTHON detector would be essentially the same but the fission and ionization chambers are not in the same plane. The numbers and letters along the edges of the array are used to identify columns and rows, respectively, of pin locations as viewed from the rear of the fork. The locations at the corners have diameters drawn through them to indicate that these are support rods, not fuel pins. The solid black locations are water channels; the gadolinium poison rods were placed in these locations of columns 3, 4, 6, and 9. The locations with small dots were locations in which the pin with ^{252}Cf and ^{137}Cs was placed.

15	Fork-Cd Data									Fork-Bare Data										
	1	2	3	4	5	6	7	8	9	1	2	3	4	5	6	7	8	9		
	A		76.200		73.850		71.900		74.180	A		62.380		64.650		65.370		62.680		
	B	97.500								B	64.480									
	C		102.10		98.480				92.420	C		79.350		85.370				80.530		
	D									D										
	E	133.30		119.90		107.60		102.80		101.50	E	98.300		97.280		94.600		93.600		90.800
	F										F									
	G		139.00		120.10		109.50		110.90		G		112.90		106.80		102.40		102.50	
	H										H									
	I	156.80				116.60		113.10			I	114.90				109.40		106.90		
	J										J									
	K		137.70		120.90		108.60		105.90		K		116.70		115.60		104.60		101.80	
	L										L									
	M	128.70		111.80		103.70		98.100		96.670	M	117.10		110.80		101.90		104.60		97.920
	N										N									
	O		96.270		89.780				85.930		O		98.850		91.020				86.900	
	P	89.700									P	91.700								
	Q			71.230		64.970		64.550		67.770	Q			75.820		72.620		67.280		68.280

Fig. 8. These are the fork cadmium-wrapped and bare fission chamber count rates (counts/s) measured with the 17 x 17 array of 3.5%-enriched uranium pins. There was no boron in the water.

Fork-Cd Data

	1	2	3	4	5	6	7	8	9
A			53.800		49.830		47.900		46.970
B	74.380								
C		80.370		67.820				59.420	
D									
E	109.30		89.780		75.550		70.470		72.070
F									
G		107.50		88.530		77.870		77.230	
H									
I	127.60				87.100		78.150		
J									
K		104.30		86.130		78.620		76.770	
L									
M	103.30		82.980		73.530		69.580		70.480
N									
O		76.120		66.980				60.170	
P	70.580								
Q			47.650		47.930		46.650		43.450

Fork-Bare Data

	1	2	3	4	5	6	7	8	9
A			36.470		33.500		33.620		32.350
B	41.950								
C		46.870		46.520				42.670	
D									
E	60.450		58.870		52.080		51.580		54.230
F									
G		68.300		65.000		61.480		58.400	
H									
I	86.570				66.400		60.220		
J									
K		76.900		66.550		63.650		61.330	
L									
M	81.380		68.280		64.420		59.030		58.080
N									
O		59.400		57.000				50.000	
P	57.870								
Q			43.080		44.220		40.730		39.800

Fig. 9. These are the fork neutron count rates for the same situation as in Fig. 8, except the boron concentration in the water was 452 ppm.

Fork-Cd Data

	1	2	3	4	5	6	7	8	9
A			45.170		39.730		36.600		36.270
B	63.420								
C		69.150		53.730				46.180	
D									
E	107.60		78.330		59.580		54.700		52.700
F									
G		95.390		73.280		63.050		59.570	
H									
I	116.30				70.580		61.450		
J									
K		98.680		75.870		61.500		59.580	
L									
M	95.330		72.480		62.050		57.230		54.330
N									
O		65.580		55.800				46.230	
P	60.650								
Q			45.450		40.120		35.800		37.650

Fork-Bare Data

	1	2	3	4	5	6	7	8	9
A			25.470		22.850		21.120		20.330
B	30.110								
C		33.650		29.620				27.450	
D									
E	44.770		42.180		35.370		34.220		32.730
F									
G		49.370		43.120		39.050		39.480	
H									
I	59.550				46.980		41.580		
J									
K		58.080		50.700		43.450		39.600	
L									
M	61.130		50.270		43.150		39.830		39.230
N									
O		45.650		41.850				34.530	
P	41.920								
Q			33.430		29.480		27.830		27.230

Fig. 10. These are the fork neutron count rates for the same situation as in Fig. 8, except the boron concentration in the water was 1010 ppm.

Fork-Cd Data

	1	2	3	4	5	6	7	8	9
A			39.550		31.420		29.930		27.880
B	63.300								
C		64.320		48.080				36.430	
D									
E	93.100		66.870		48.530		44.800		44.230
F									
G		86.800		64.330		51.920		47.930	
H									
I	108.70				57.020		51.180		
J									
K		81.800		63.170		50.080		46.690	
L									
M	83.430		63.300		48.600		41.150		41.130
N									
O		55.190		44.730				33.450	
P	55.020								
Q			36.570		29.900		27.440		26.240

Fork-Bare Data

	1	2	3	4	5	6	7	8	9
A			17.250		14.600		13.480		13.680
B	22.700								
C		24.880		21.620				17.230	
D									
E	31.620		28.700		24.300		22.580		22.960
F									
G		35.250		31.780		27.470		24.480	
H									
I	42.400				29.870		27.320		
J									
K		41.780		33.300		29.050		26.230	
L									
M	46.170		36.680		29.600		24.930		23.950
N									
O		32.130		27.720				22.220	
P	30.720								
Q			22.820		20.000		17.900		17.360

Fig. 11. These are the fork neutron count rates for the same situation as in Fig. 8, except the boron concentration in the water was 2070 ppm.

Fork-Cd Data

	1	2	3	4	5	6	7	8	9
A			38.290		28.230		24.970		25.160
B	59.170								
C		58.330		43.470				30.780	
D									
E	89.220		64.070		45.330		38.910		37.680
F									
G		81.870		56.370		45.870		39.060	
H									
I	99.990				53.430		42.670		
J									
K		78.930		56.370		42.680		38.730	
L									
M	76.400		55.620		43.070		36.540		36.310
N									
O		51.700		41.180				29.430	
P	51.200								
Q			32.410		26.220		23.160		23.520

Fork-Bare Data

	1	2	3	4	5	6	7	8	9
A			13.040		11.100		9.9900		9.3400
B	20.130								
C		19.070		17.020				12.230	
D									
E	28.050		22.480		18.430		16.390		16.490
F									
G		30.270		23.900		20.170		17.950	
H									
I	42.000				24.750		21.010		
J									
K		36.230		26.700		22.380		19.060	
L									
M	37.950		28.870		23.270		18.940		18.550
N									
O		28.200		22.200				16.080	
P	26.970								
Q			19.360		15.630		13.630		12.930

Fig. 12. These are the fork neutron count rates for the same situation as in Fig. 8, except the boron concentration in the water was 3060 ppm.

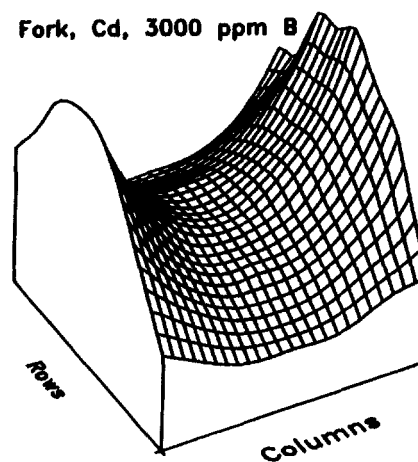
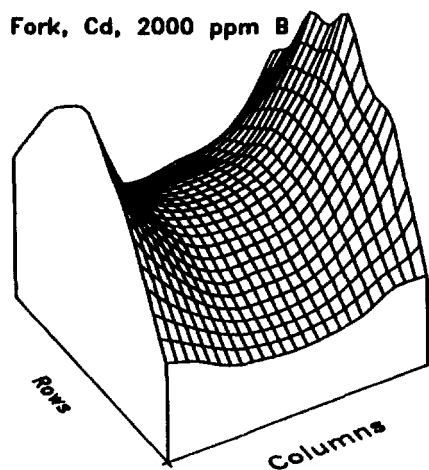
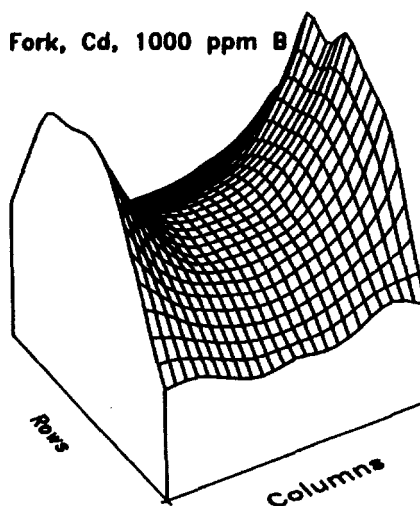
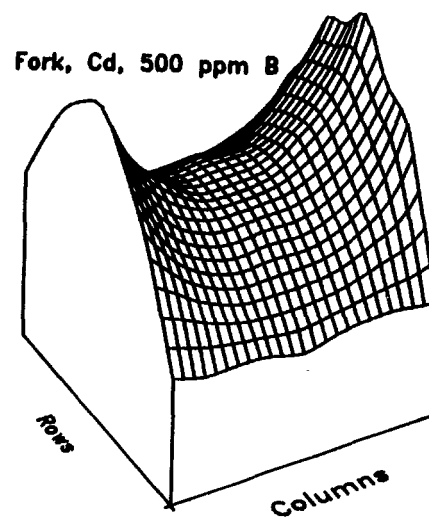
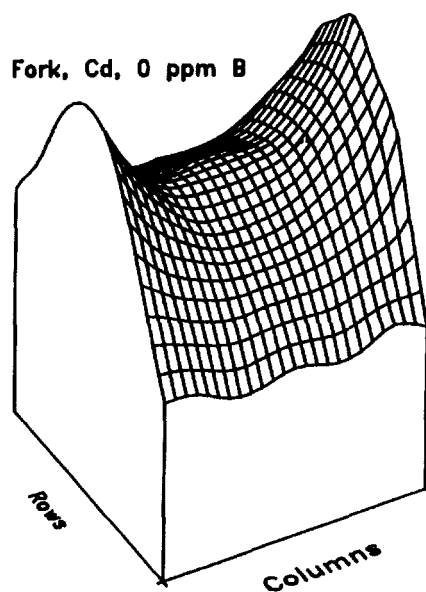


Fig. 13. The count rates with cadmium-wrapped fission chambers (Figs. 8-12) are shown graphically. The scales of diagrams are all the same, so the effects of different boron concentrations can be seen qualitatively. Count rates for columns 10-17 (where no measurements were taken) were set equal to those from columns 8-1, respectively. The ripples along the borders are artifacts of the interpolation process used in generating the diagrams.

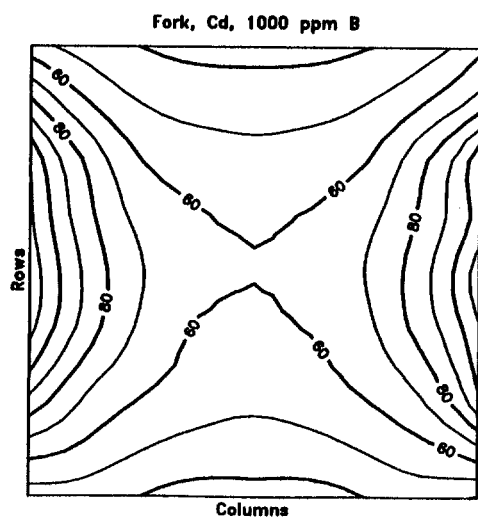
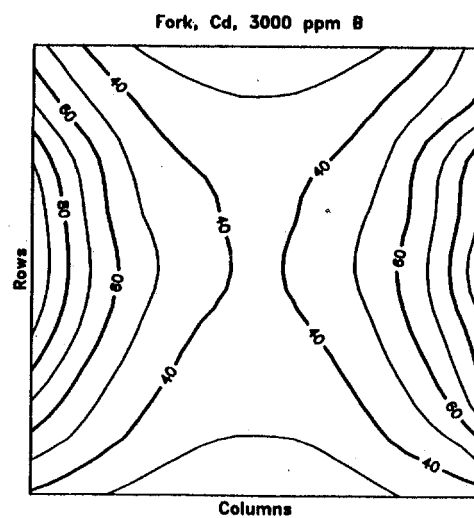
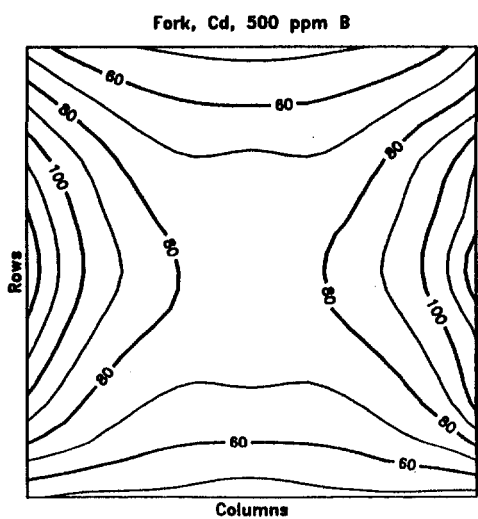
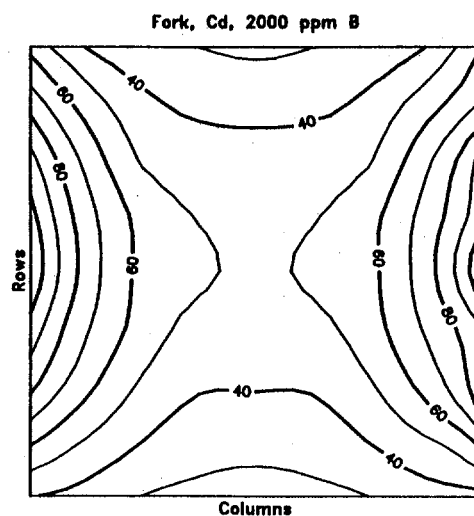
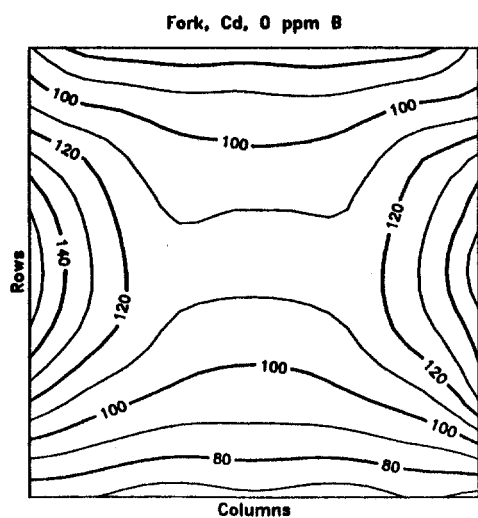
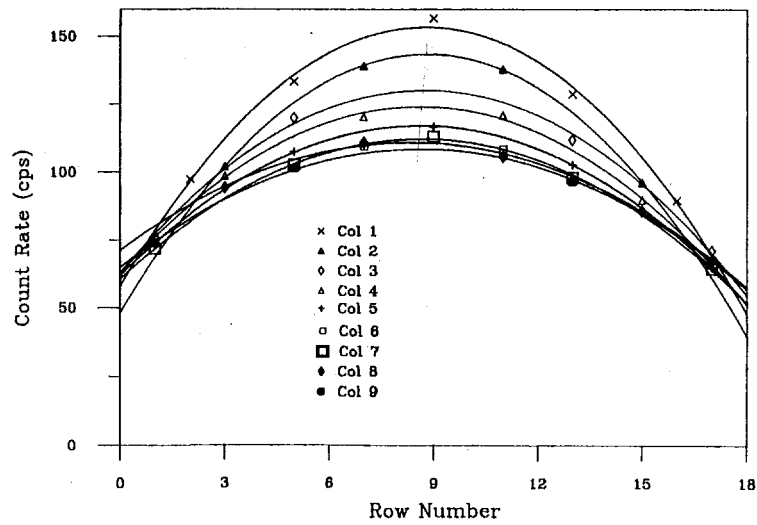
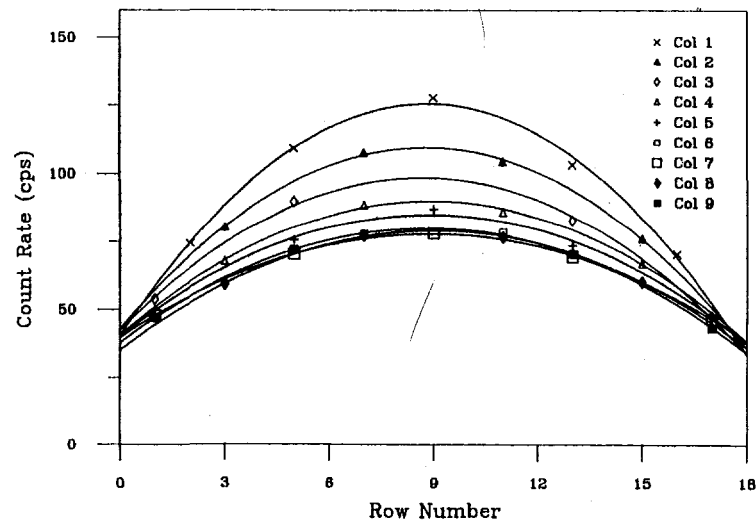


Fig. 14. The data with cadmium-wrapped fission chambers (Figs. 8-12) are used to generate contour plots of count rates at different boron concentrations. Count rates for columns 10-17 were set equal to those from columns 8-1, respectively.

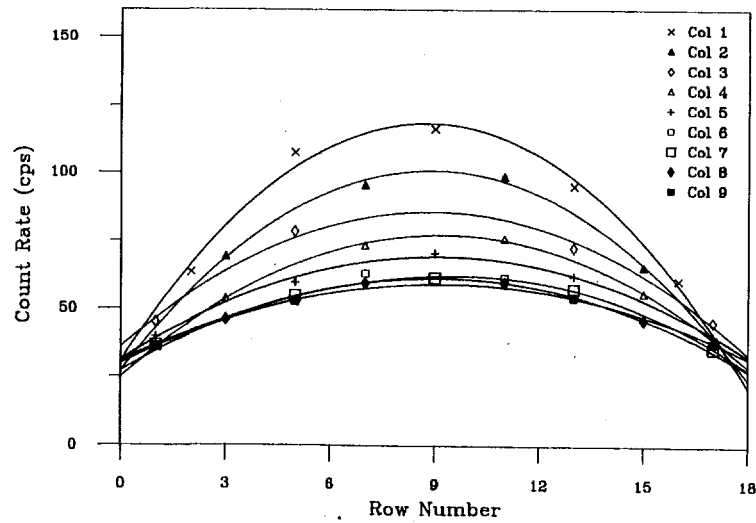
Fork Column Profiles, 0 ppm B



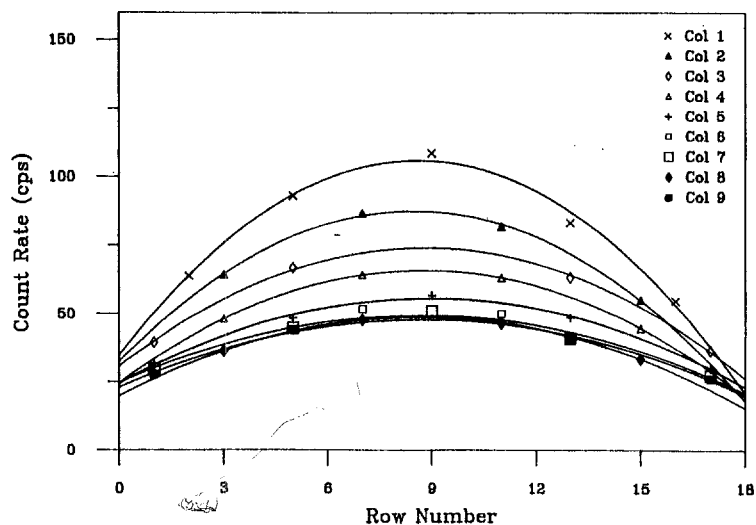
Fork Column Profiles, 500 ppm



Fork Column Profiles, 1000 ppm B



Fork Column Profiles, 2000 ppm B



Fork Column Profiles, 3000 ppm B

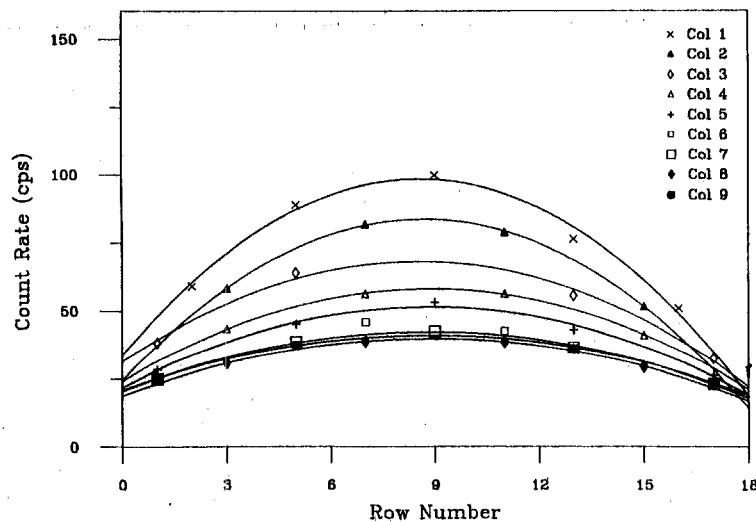
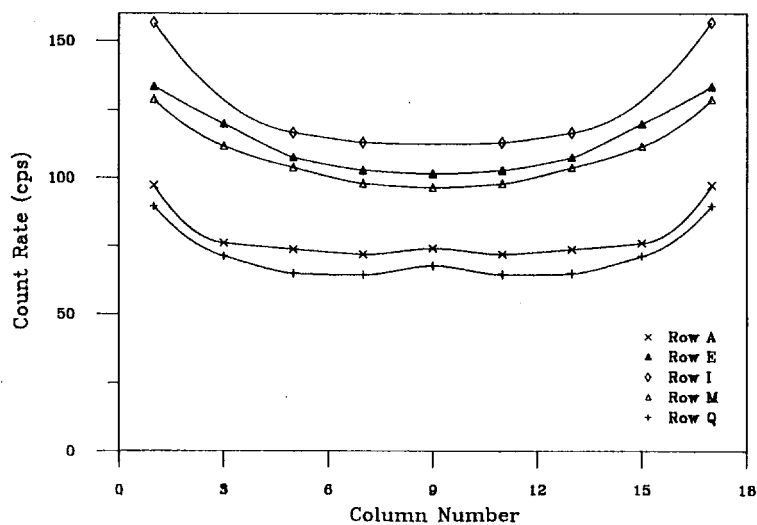
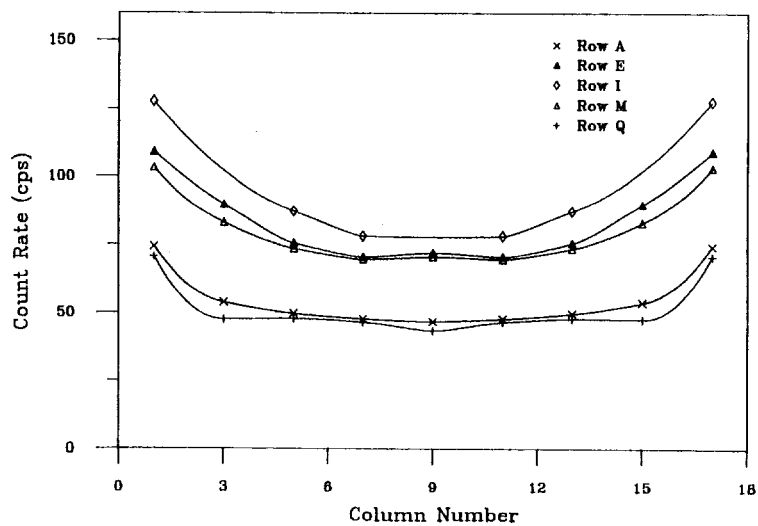


Fig. 15. The fork data of Figs. 8-12 from cadmium-wrapped fission chambers are shown graphically. The curves connect the data from pins in the same column; the curves have no significance beyond helping the viewer organize the data. Columns nearest the fork's tines produced the highest count rates.

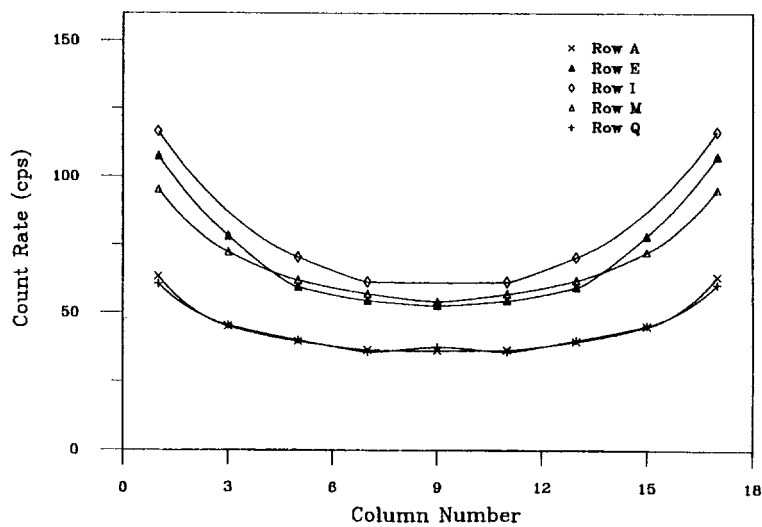
Fork Row Profiles, 0 ppm B



Fork Row Profiles, 500 ppm B



Fork Row Profiles, 1000 ppm B



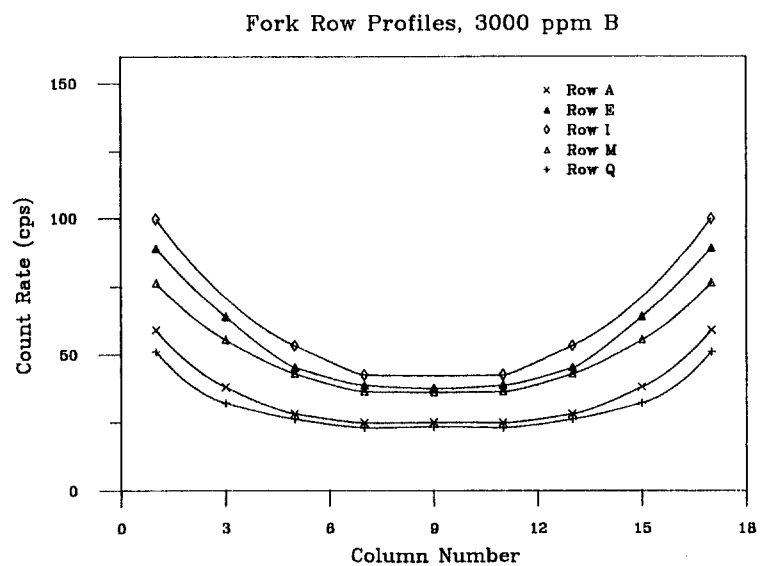
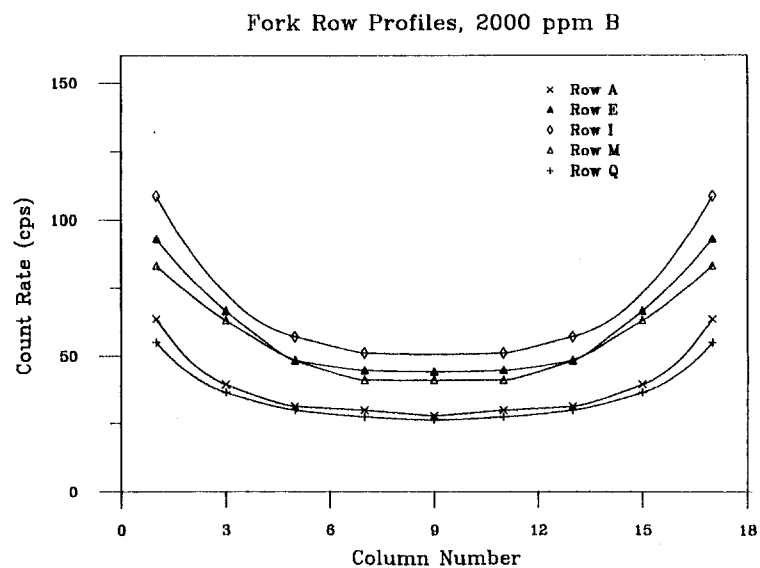
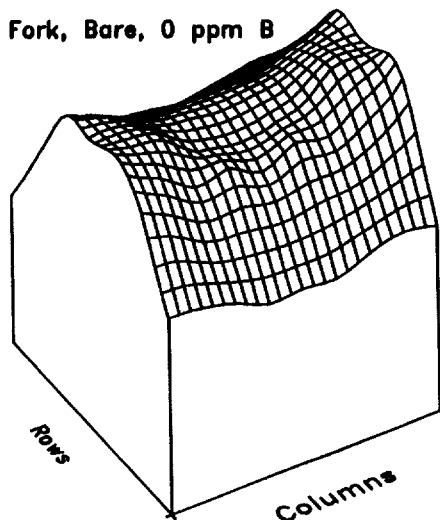
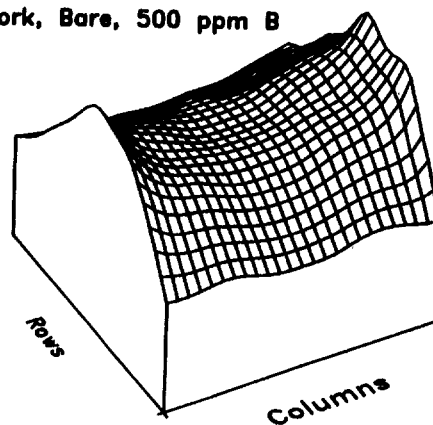


Fig. 16. Same as Fig. 15, except that data from the same rows are shown connected by curves.

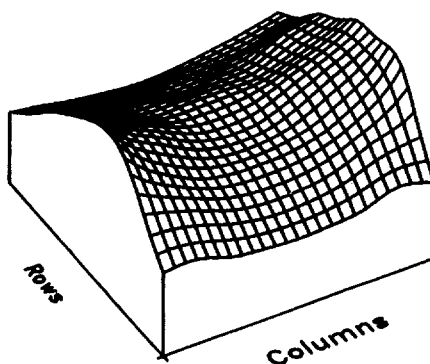
Fork, Bare, 0 ppm B



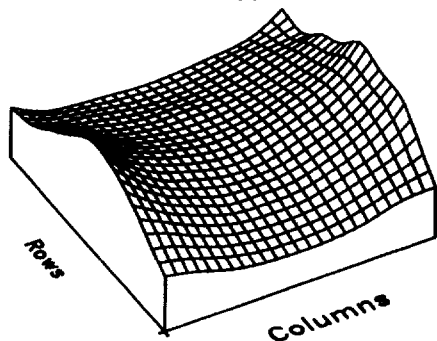
Fork, Bare, 500 ppm B



Fork, Bare, 1000 ppm B



Fork, Bare, 3000 ppm B



Fork, Bare, 2000 ppm B

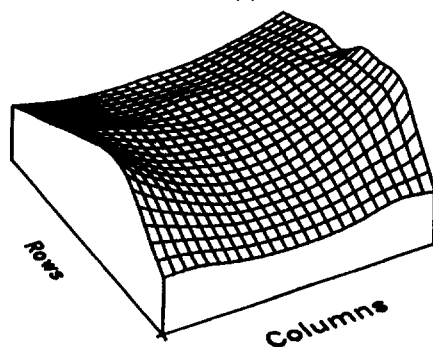


Fig. 17. The count rates with bare fission chambers (Figs. 8-12) are shown graphically. The scales of the diagrams are all the same, so the effects of different boron concentrations can be seen qualitatively. Count rates for columns 10-17 (where no measurements were taken) were set equal to those from columns 8-1, respectively. The ripples along the borders are artifacts of the interpolation process used in generating the diagrams.

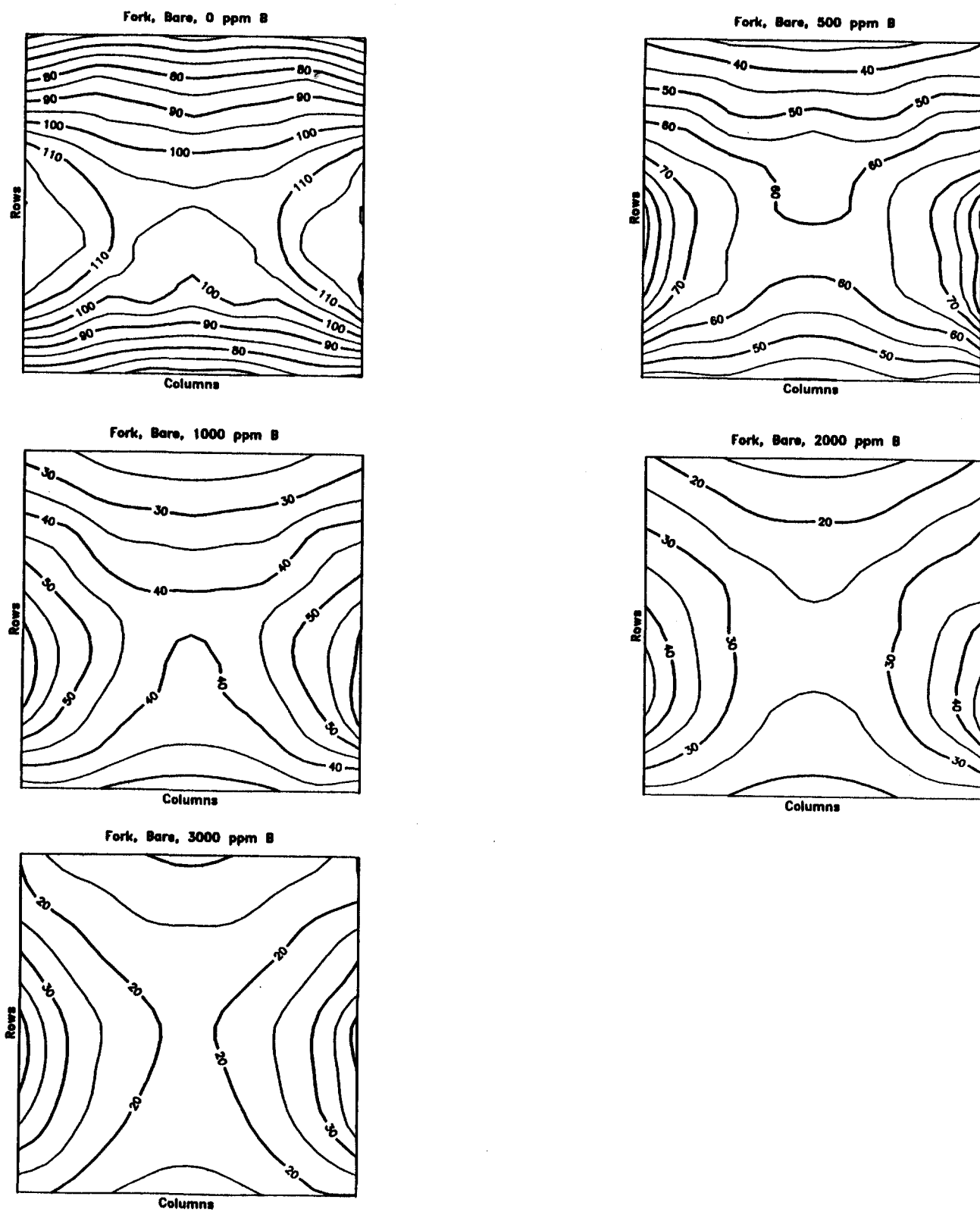
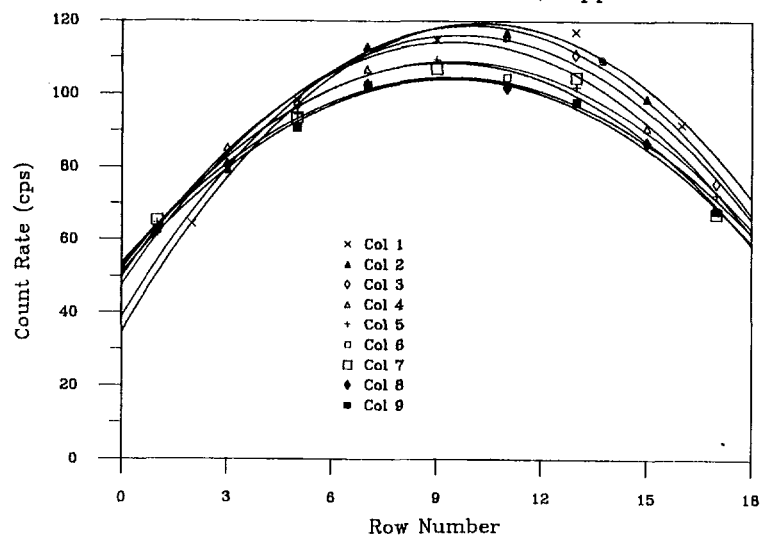
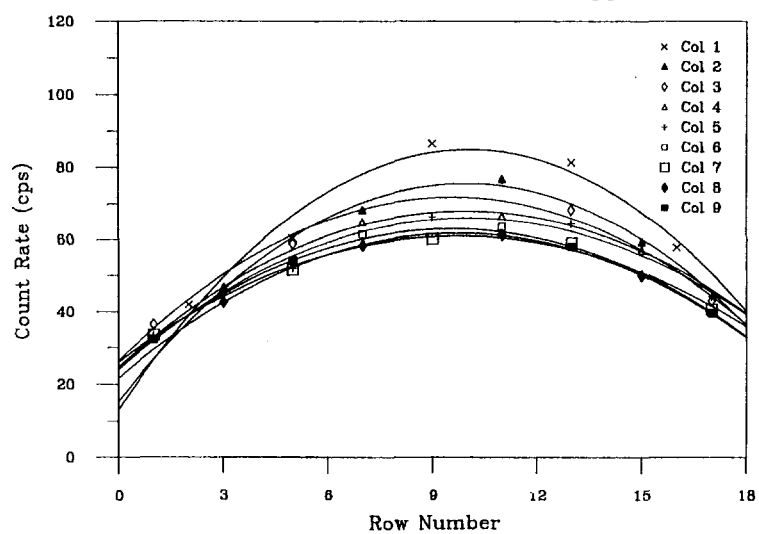


Fig. 18. The data with bare fission chambers (Figs. 8-12) are used to generate contour plots of count rates at different boron concentrations. Count rates for columns 10-17 were set equal to those from columns 8-1, respectively.

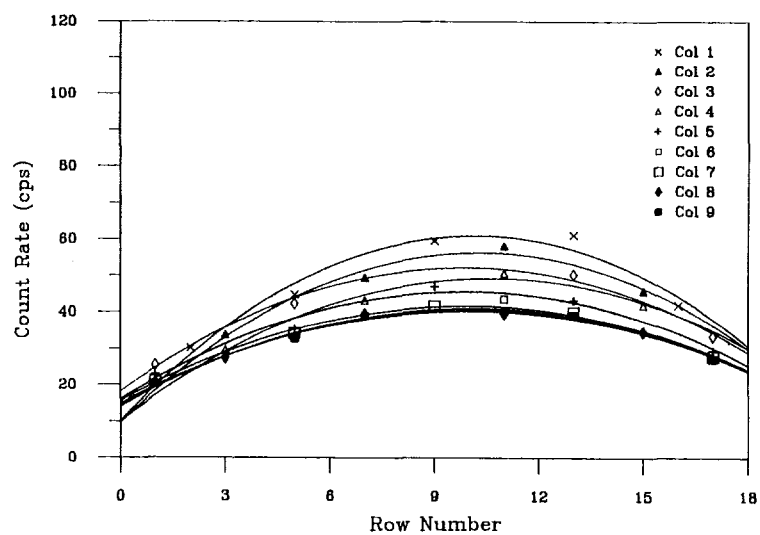
Fork-Bare Column Profiles, 0 ppm B



Fork-Bare Column Profiles, 500 ppm B



Fork-Bare Column Profiles, 1000 ppm B



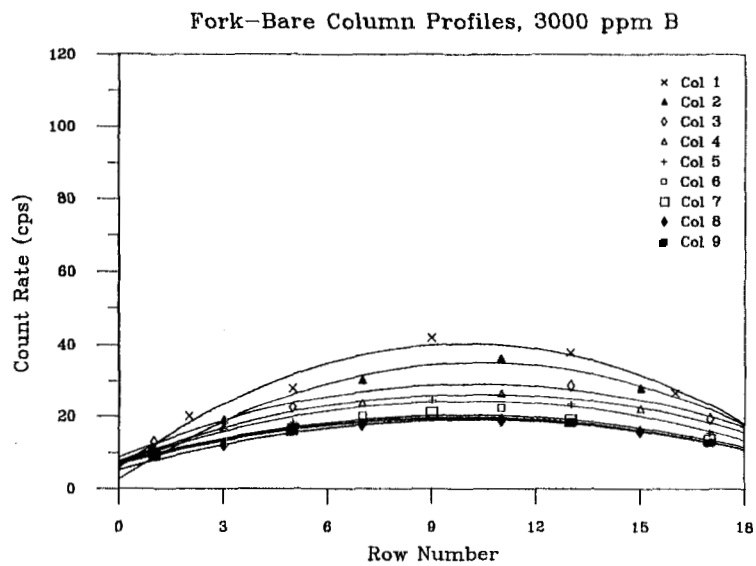
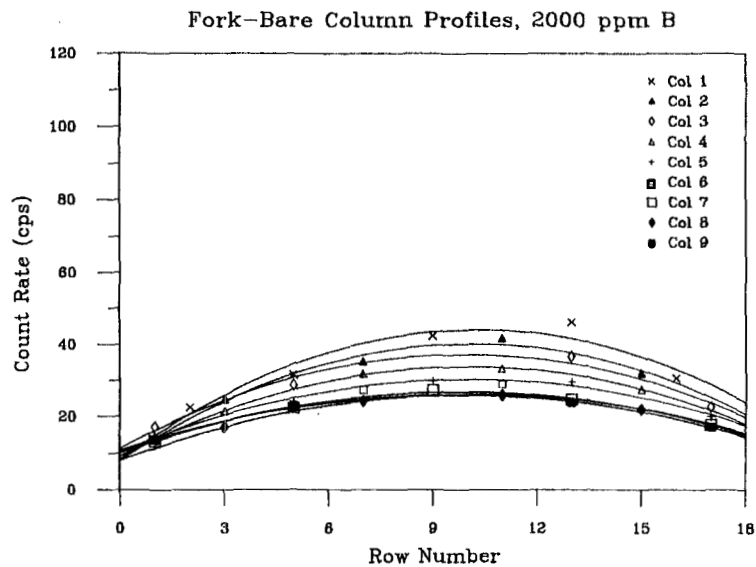
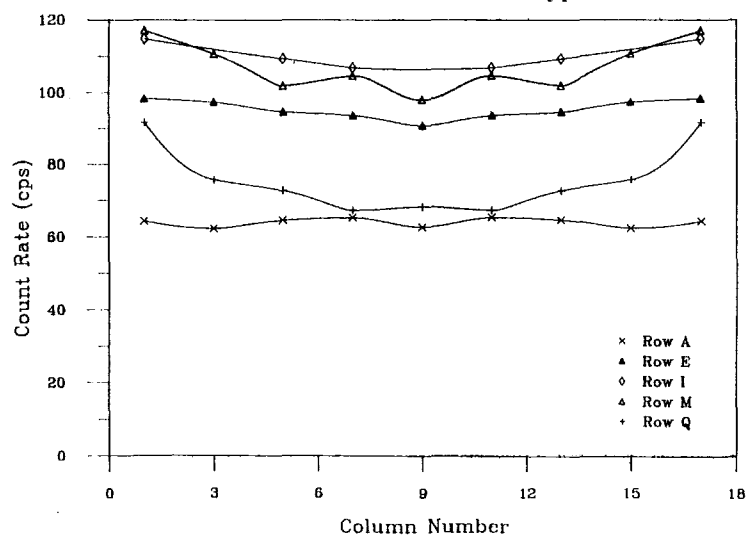
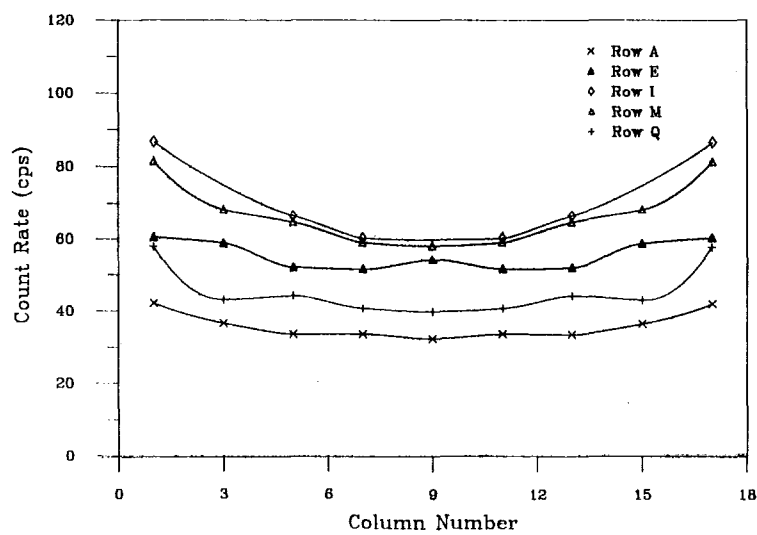


Fig. 19. The fork data of Figs. 8-12 from bare fission chambers are shown graphically. The curves connect the data from pins in the same column; the curves have no significance beyond helping the viewer organize the data. Columns nearest the fork's tines produced the highest count rates.

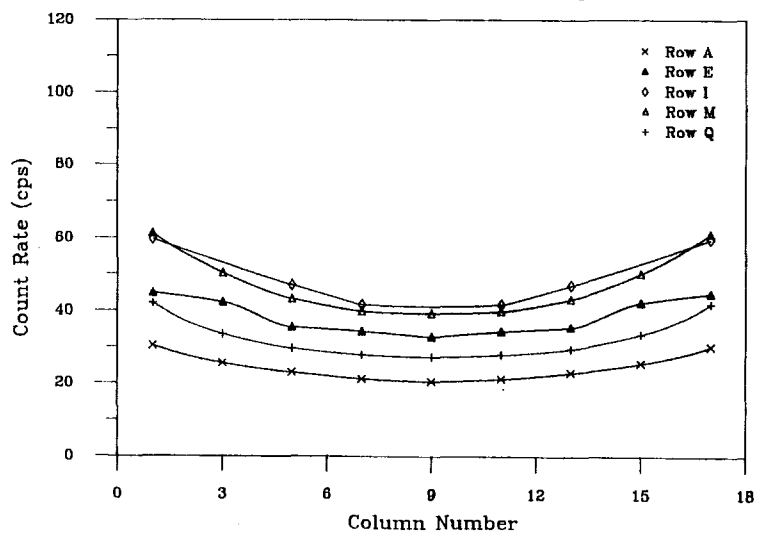
Fork-Bare Row Profiles, 0 ppm B



Fork-Bare Row Profiles, 500 ppm B



Fork-Bare Row Profiles, 1000 ppm B



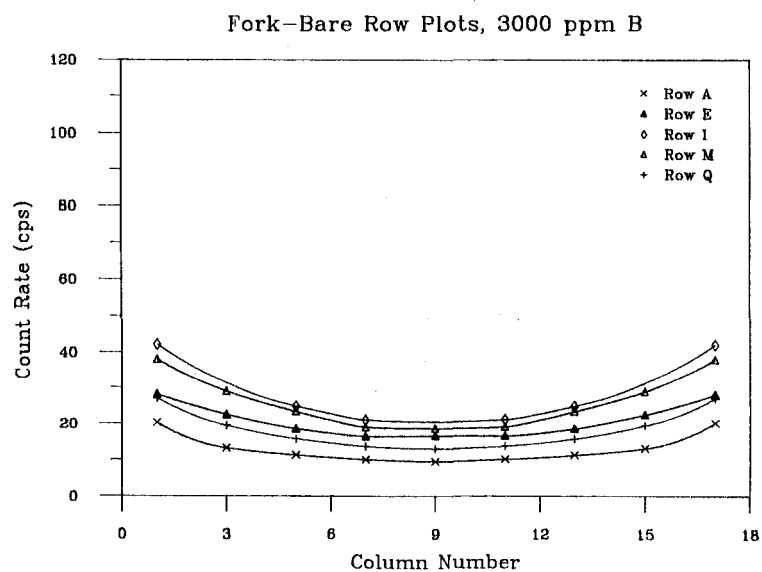
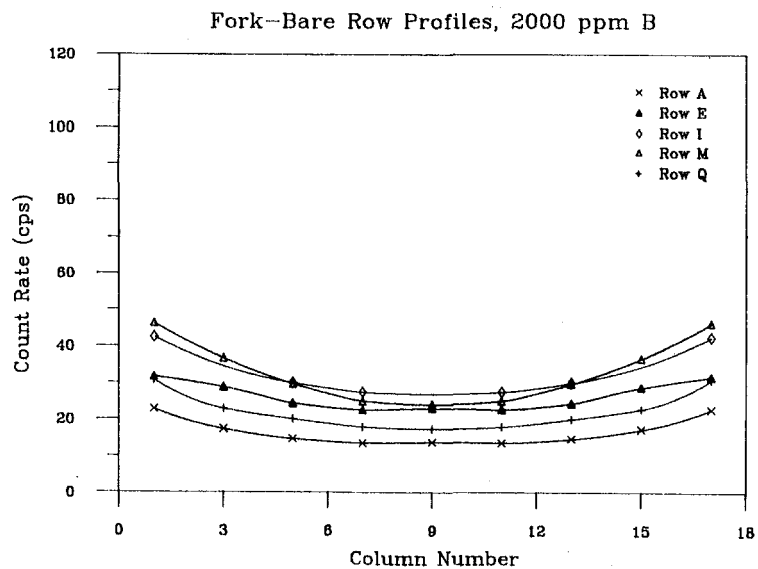
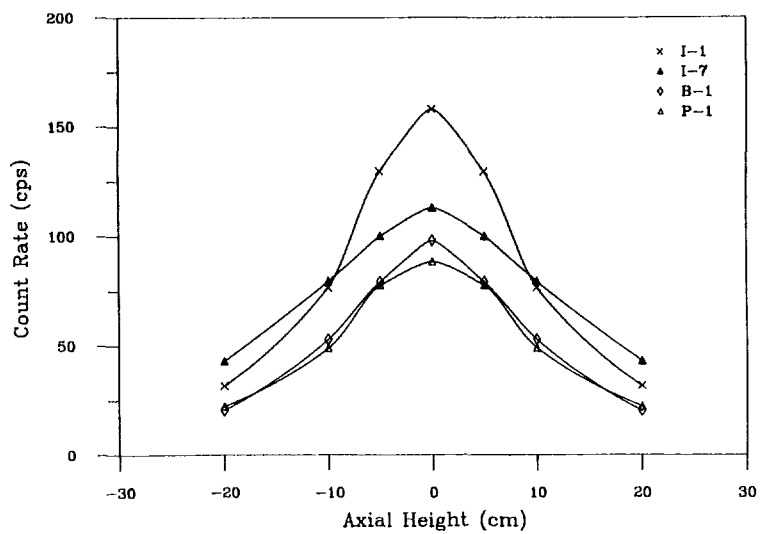
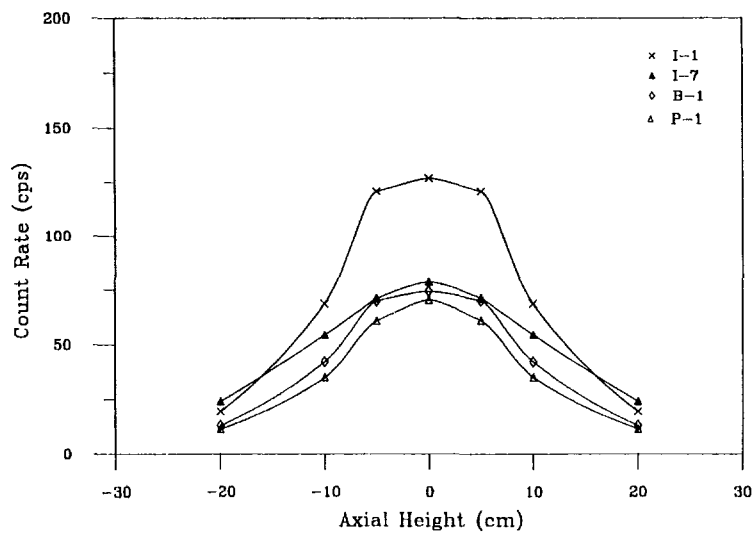


Fig. 20. The caption to Fig. 19 applies here, except that data from the same rows are shown connected by curves.

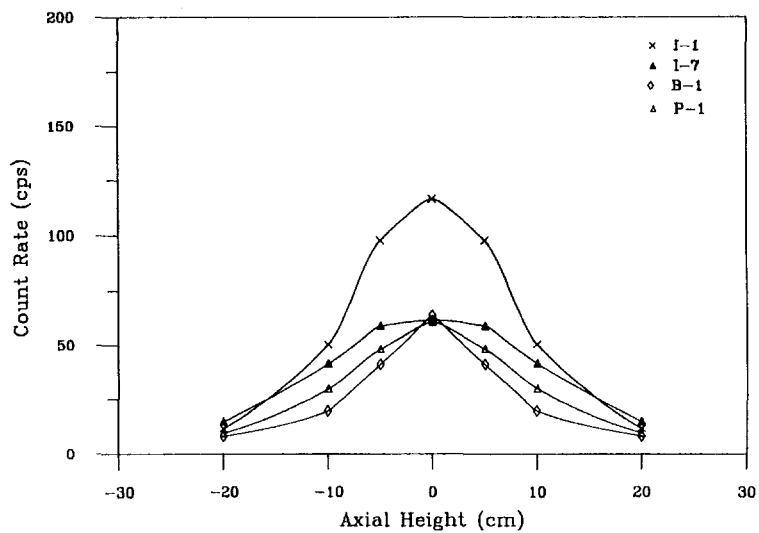
Fork-Cd Axial Profiles, 0 ppm B



Fork-Cd Axial Profiles, 500 ppm B



Fork-Cd Axial Profiles, 1000 ppm B



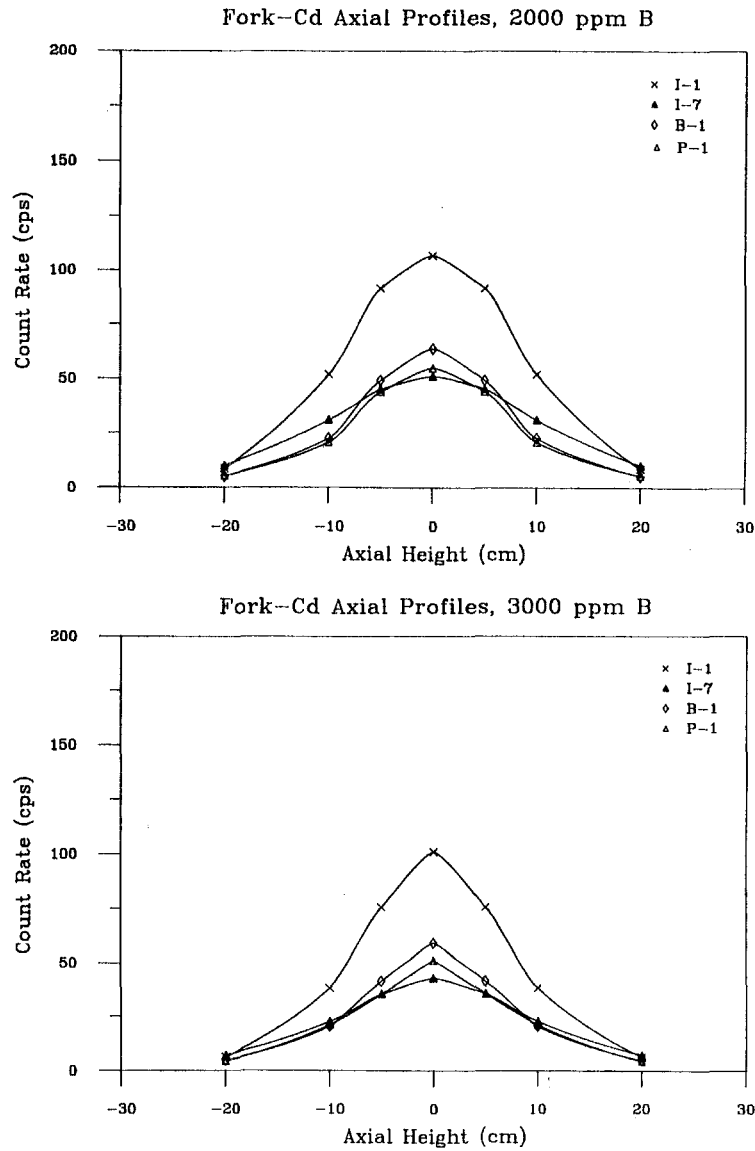
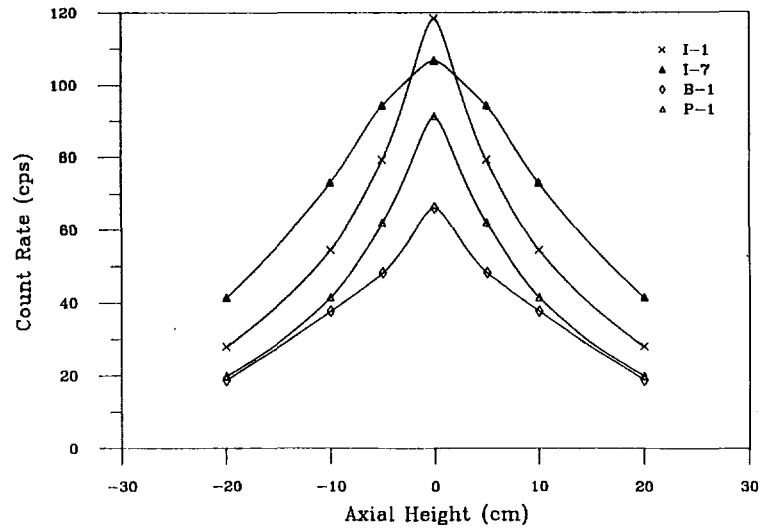
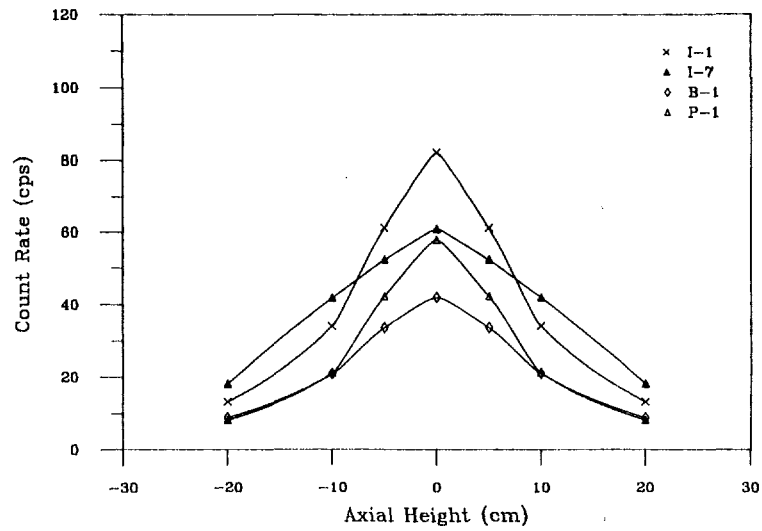


Fig. 21. The fork neutron axial profile data from Table II for the cadmium-wrapped fission chambers are shown here. Data were taken at only positive vertical displacements, but the same data were used at negative displacements to generate these symmetrical profiles.

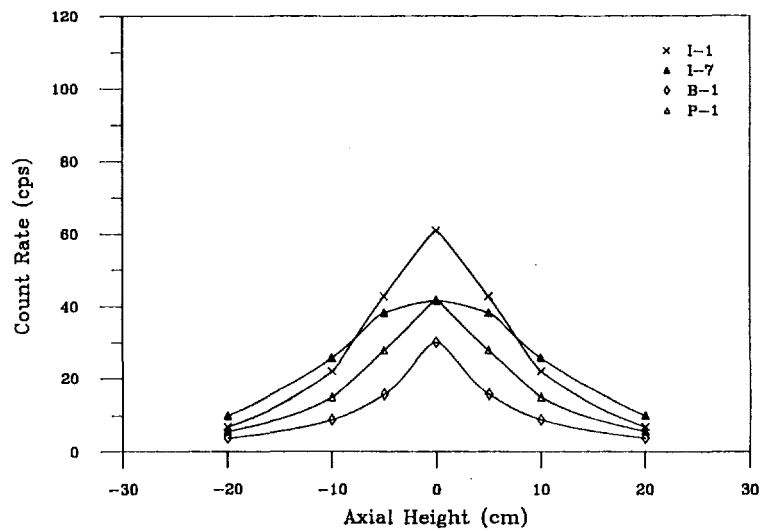
Fork-Bare Axial Profiles, 0 ppm B



Fork-Bare Axial Profiles, 500 ppm B



Fork-Bare Axial Profiles, 1000 ppm B



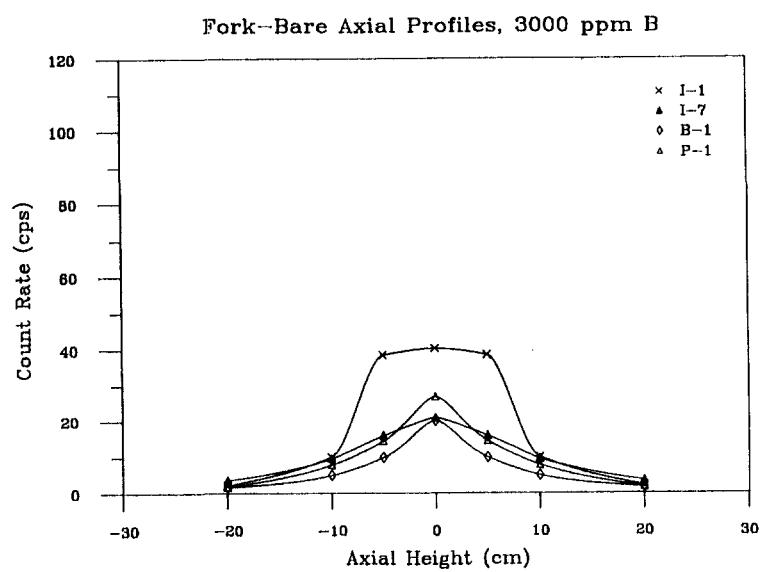
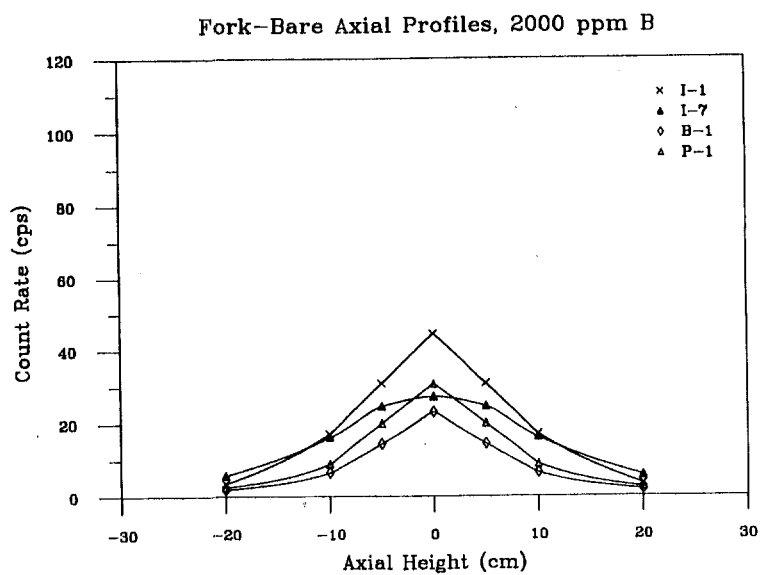


Fig. 22. The caption to Fig. 21 applies here, except the data are from the bare fission chambers.

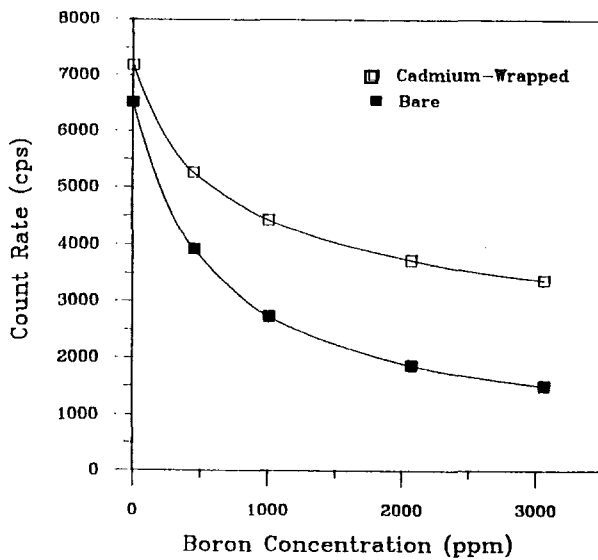


Fig. 23. Sums of fork count rates from Figs. 8-12 are displayed graphically and given numerically in Table VII. The count rates expected from columns 10-17 (where no measurements were taken) are set equal to the count rates in columns 1-8. The cadmium-wrapped data are the larger of the two, indicating that the thermal flux at the fork detector is much lower than the epithermal flux.

Cd
Bare
Cd/Bare

	1	2	3	4	5	6	7	8	9
A									
B									
C									
D									
E			85.680		72.250				
F			68.320		61.120				
G			1.2541		1.1821				
H									
I	131.00				81.970		76.400		
J	89.440				77.150		71.070		
K	1.4647				1.0625		1.0750		
L									
M			80.520		69.960				
N			81.120		71.450				
O			.99260		.97915				
P									
Q									

Fig. 24. The fork neutron count rates from seven pin locations are shown with gadolinium poison rods inside the array. At each position the three numbers are the count rate from the cadmium-covered fission chambers, bare fission chambers, and their ratio.

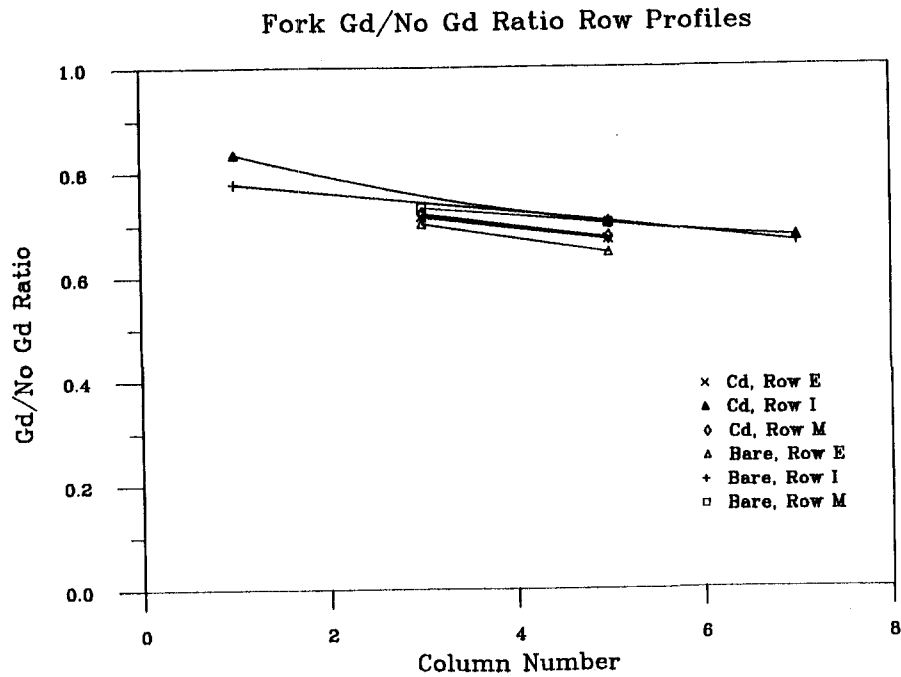


Fig. 25. Ratios of fork count rates with and without gadolinium poison rods present are shown. These ratios decrease slowly as the source moves toward the interior of the assembly. No boron was present during these measurements.

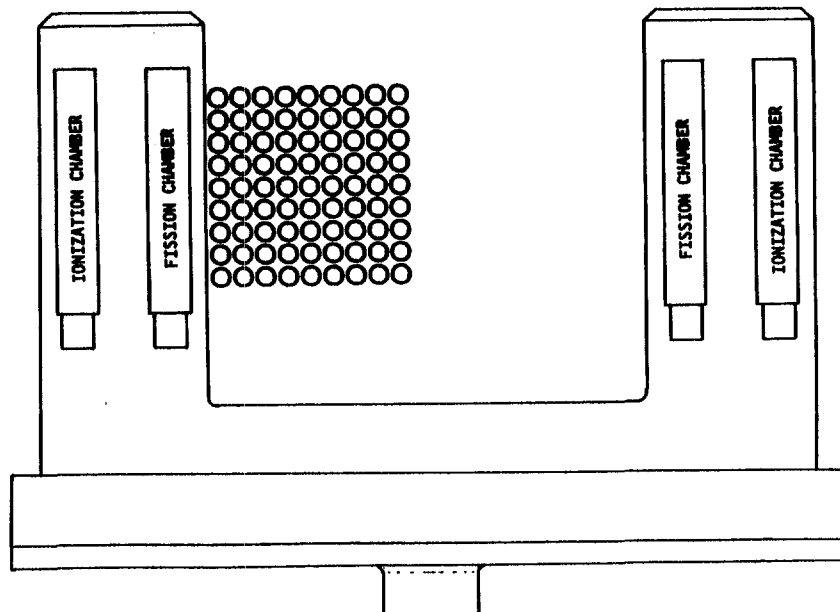


Fig. 26. The 9 x 9 array of pins was studied and positioned next to a fork tine. The center pin of the array was at location H-5 of Fig. 7.

0.25%
3.50%
0.25/3.50

	1	2	3	4	5	6	7	8	9
A									
B									
C									
D									
E									
F									
G					29.120 52.560 .55403				
H	90.400 108.30 .83472	67.550 87.210 .77457	52.410 73.370 .71432	38.030 61.910 .61428	29.780 52.540 .56681	23.160 46.750 .49540	18.430 42.300 .43570	17.230 37.830 .45546	16.590 33.720 .49199
I					29.690 53.180 .55829				

Fig. 27. Neutron count rates with the 9 x 9 array and the cadmium-wrapped fission chambers of the fork detector are shown here. At each source location three numbers are shown; from top to bottom they are the count rate with depleted uranium pins, the count rate with 3.5%-enriched uranium pins, and the ratio of depleted count rate to enriched count rate. The source was placed in each position of row H that goes through the middle of the array.

0.25%
3.50%
0.25/3.50

	1	2	3	4	5	6	7	8	9
A									
B									
C									
D									
E									
F									
G					33.870 58.060 .58336				
H	58.730 80.620 .72848	53.080 81.560 .65081	48.020 75.070 .63967	39.860 65.460 .60892	34.360 58.230 .59007	30.640 55.360 .55347	26.170 50.260 .52069	25.810 47.960 .53816	27.770 46.480 .59746
I					35.680 60.130 .59338				

Fig. 28. The caption of Fig. 27 applies here, except that the data are from the bare fission chambers.

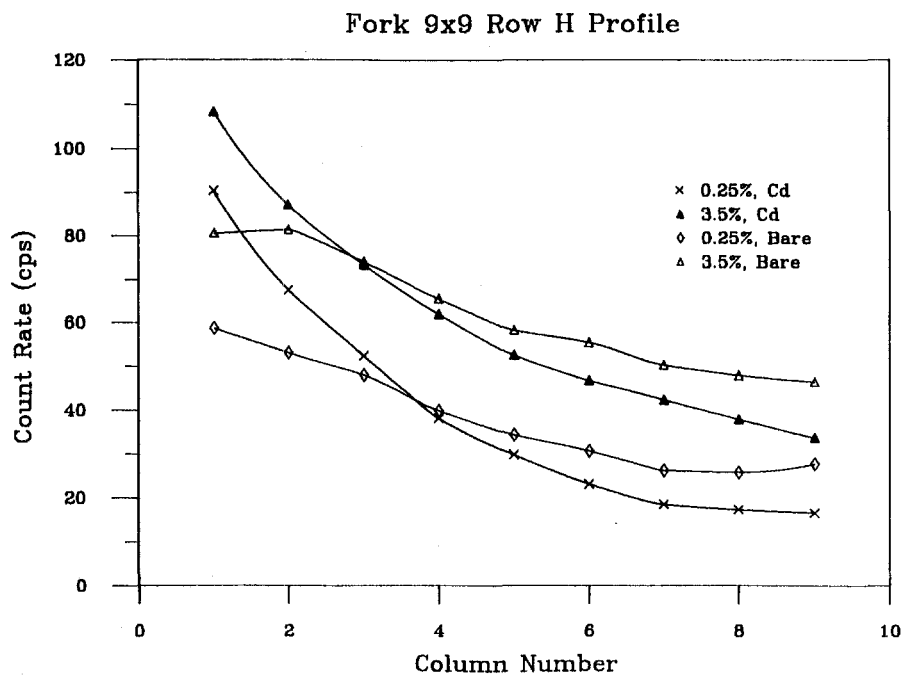


Fig. 29. The fork data of Figs. 27-28 are shown graphically. Each curve has a different combination of enrichment and fission chamber, as given in the legend. The effect of multiplication is readily seen by comparing the two cadmium-wrapped curves with different enrichments or the two bare curves.

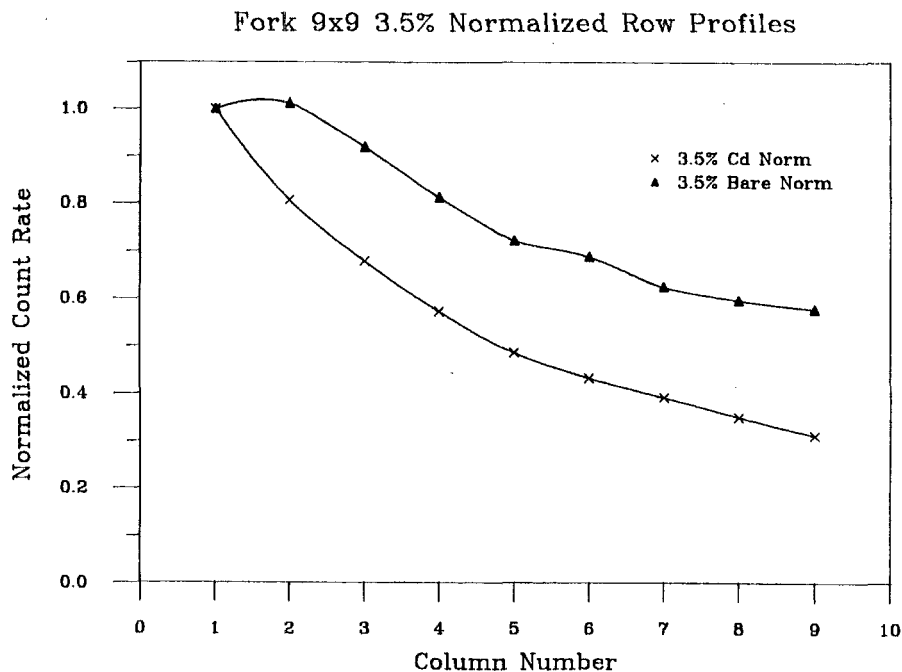


Fig. 30. To view the effects of multiplication within the arrays in a different way, the data of Fig. 27-28 for enriched uranium pins are normalized to the count rate at column 1 (nearest the fork's tine). These data should be compared with those in Fig. 31.

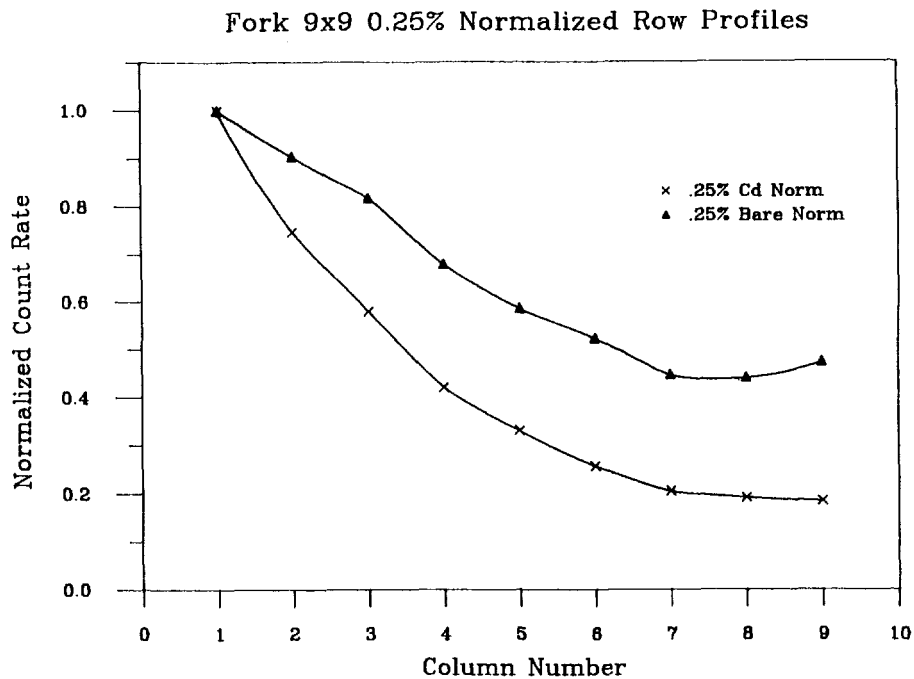


Fig. 31. The fork data of Figs. 27-28 for depleted uranium pins are shown here after being normalized to the values in column 1. When compared with the curves of Fig. 30, these count rates decrease rapidly as the neutron source moves to the array's interior. There is a slight rise at column 9 in the data for the fission chamber without cadmium; at this point there is only water between the ^{252}Cf source and the fission chambers in one of the fork's tines (see Fig. 26), so this geometry is apparently enhancing the thermal neutron detection.

	1	2	3	4	5	6	7	8	9
A		.00340	.00220	.00130					
B	.00740		.00240	.00150					
C	.00800	.00530	.00330	.00160					
D									
E	.01240	.00600	.00410	.00310	.00140	.00090			
F				.00280	.00170		.00068		
G	.01530	.00800	.00440	.00240	.00170	.00095	.00070		
H			.00490	.00290					
I	.01570	.00880		.00380	.00230		.00110		
J									
K	.01560	.00840							
L									
M	.01340	.00740							
N									
O	.01020	.00570							
P	.00930								
Q		.00370							

Fig. 32. These fork gamma-ray data are the GRAND-I readings (proportional to the current through the ionization chambers) from a ^{137}Cs source at the locations indicated by the presence of the data. Uncertainties (1σ) are generally about 0.0003.

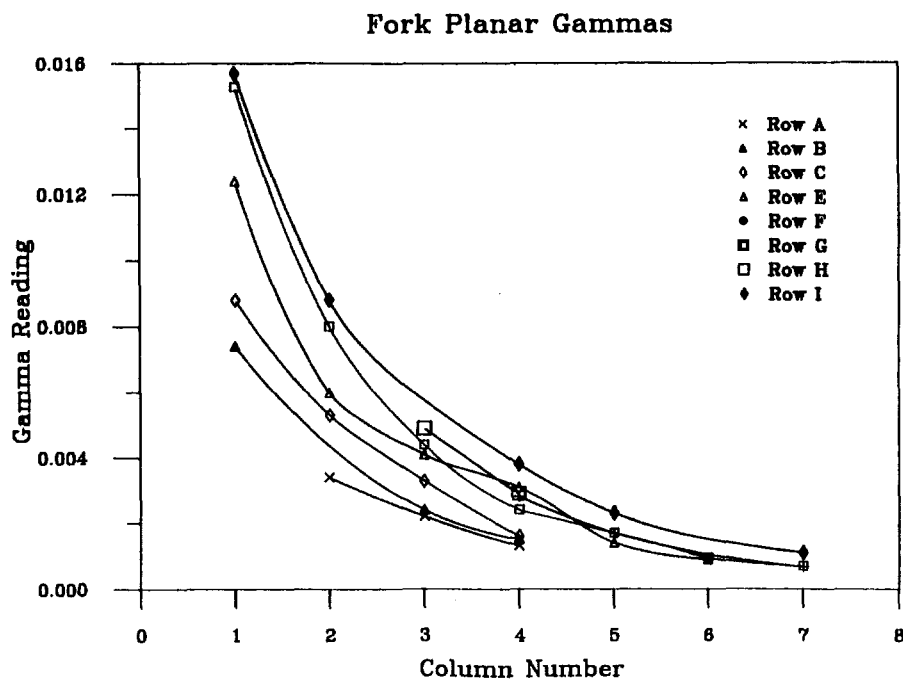


Fig. 33. The fork gamma-ray data of Fig. 32 are shown graphically. The curves connect data from pins in a common row (see Fig. 7). The higher data values are from the column nearest the fork's tine. All the curves are nearly exponential, even when one or two water channels are present; the coefficients of exponential curves fitted to these data are listed in Table VIII.

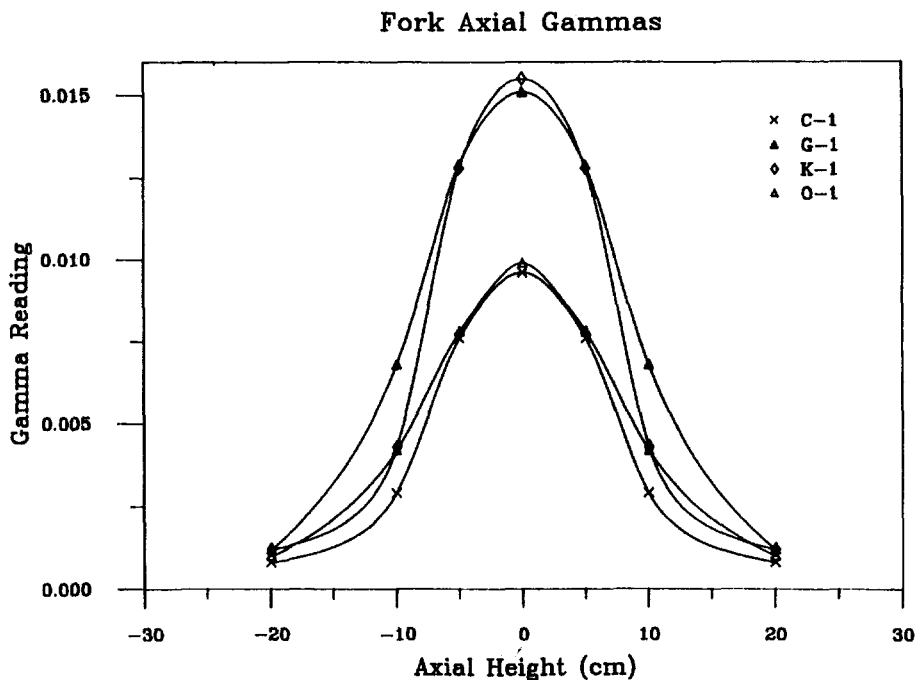


Fig. 34. The fork gamma-ray axial profile data of Table IX are shown. Data were taken at only positive vertical displacements, but the same data were used at negative displacements to generate these symmetric profiles.

TABLE II. Axial Fork Neutron Data at 0 ppm Boron.
Uncertainties are $\sqrt{(\text{Count Rate}/60)}$

Vertical Distance (cm)	Counts per Second							
	I-1		B-1		P-1		I-7	
	Cd-FC	Bare-FC	Cd-FC	Bare-FC	Cd-FC	Bare-FC	Cd-FC	Bare-FC
0	158.1	118.4	98.02	66.05	88.53	91.22	113.1	106.9
5	129.6	79.25	79.27	48.25	77.90	61.95	100.2	94.30
10	76.90	54.45	53.00	37.65	49.20	41.42	79.67	73.00
20	31.90	28.05	20.55	18.92	22.52	19.98	43.30	41.40

TABLE III. Axial Fork Neutron Data at 452 ppm Boron.
Uncertainties are $\sqrt{(\text{Count Rate}/60)}$

Vertical Distance (cm)	Counts per Second							
	I-1		B-1		P-1		I-7	
	Cd-FC	Bare-FC	Cd-FC	Bare-FC	Cd-FC	Bare-FC	Cd-FC	Bare-FC
0	127.1	82.00	74.38	41.95	70.58	57.87	78.85	60.82
5	120.9	61.17	70.12	33.70	61.17	42.27	71.45	52.32
10	68.92	34.15	42.28	21.05	35.22	21.27	54.67	41.90
20	19.58	13.30	13.02	8.93	11.57	8.25	24.20	18.25

TABLE IV. Axial Fork Neutron Data at 1010 ppm Boron.
Uncertainties are $\sqrt{(\text{Count Rate}/60)}$

Vertical Distance (cm)	Counts per Second							
	I-1		B-1		P-1		I-7	
	Cd-FC	Bare-FC	Cd-FC	Bare-FC	Cd-FC	Bare-FC	Cd-FC	Bare-FC
0	116.8	60.95	63.42	30.11	60.65	41.92	61.45	41.58
5	97.90	42.85	40.95	15.70	48.20	27.87	58.92	38.30
10	50.52	22.03	19.77	8.95	29.85	14.93	41.53	25.78
20	11.87	6.88	8.17	3.77	9.62	5.62	15.20	10.10

TABLE V. Axial Fork Neutron Data at 2070 ppm Boron.
Uncertainties are $\sqrt{(\text{Count Rate}/60)}$

Vertical Distance (cm)	Counts per Second							
	I-1		B-1		P-1		I-7	
	Cd-FC	Bare-FC	Cd-FC	Bare-FC	Cd-FC	Bare-FC	Cd-FC	Bare-FC
0	106.9	44.40	63.82	23.06	55.02	30.72	51.18	27.32
5	91.78	30.93	49.22	14.40	44.05	20.03	45.28	24.69
10	52.07	17.15	22.55	6.63	20.80	8.94	31.02	16.17
20	8.60	3.61	5.21	1.88	5.40	2.48	10.12	5.85

TABLE VI. Axial Fork Neutron Data at 3060 ppm Boron.
Uncertainties are $\sqrt{(\text{Count Rate}/60)}$

Vertical Distance (cm)	Counts per Second							
	I-1		B-1		P-1		I-7	
	Cd-FC	Bare-FC	Cd-FC	Bare-FC	Cd-FC	Bare-FC	Cd-FC	Bare-FC
0	101.0	40.30	59.17	20.13	51.20	26.97	42.67	21.01
5	75.83	38.48	41.34	9.87	35.60	14.52	35.48	15.97
10	38.22	10.01	20.44	4.84	21.13	7.74	22.80	9.54
20	6.40	2.03	4.72	1.62	4.37	1.65	7.29	3.41

TABLE VII. Sums of Neutron Data.
Count rates in columns 1-8 are doubled.
Axial factor of 1.4 for PYTHON data.

Boron (ppm)	Cd-Wrapped	Bare	PYTHON	<u>Fork-Cd</u> PYTHON
0	7180	6518	2619	2.742
500	5261	3914	1717	3.063
1000	4433	2733	1433	3.094
2000	3730	1876	1180	3.160
3000	3370	1504	1064	3.168

TABLE VIII. Gamma-Ray Attenuation Coefficients at 662 keV.
Fork Gamma Reading = $a e^{-\mu x}$

Pin Row	a (GRAND-I units)	μ (cm^{-1})
A	0.008686	0.4664
B	0.01282	0.5527
C	0.01489	0.5211
E	0.02079	0.5470
F	0.02239	0.5450
G	0.02784	0.6074
H	0.02950	0.5968
I	0.02641	0.5089
K	0.02897	0.6190
M	0.02427	0.5938
O	0.01825	0.5819
P	0.01517	0.4896

TABLE IX. Axial Fork Gamma-Ray Data

Vertical Distance (cm)	C-1 ^a	G-1 ^a	K-1 ^a	O-1 ^a
0	0.0096(3)	0.0151(3)	0.0155(4)	0.0099(3)
5	0.0076(2)	0.0129(4)	0.0128(3)	0.0078(3)
10	0.0029(2)	0.0068(3)	0.0043(2)	0.0042(3)
20	0.0008(3)	0.0012(2)	0.0012(2)	0.0010(2)

^aUncertainty in the last figure is shown in parentheses.

IV. PYTHON MEASUREMENTS

A. Neutron Measurements

Neutron measurements were taken with the PYTHON detector that parallel those described in Section III for the fork.

1. Standard Assembly

a. **Boron Effects.** The numerical data with the ^{252}Cf source in the plane of the fission chambers are given in Figs. 35-39 and shown graphically in Figs. 40-43 for various columns and rows. Axial profiles are given in Tables X-XIV and Fig. 44.

Sums of count rates at different boron concentrations are given in Table VII and plotted in Fig. 45.

b. **Gadolinium Poison Effects.** The count rates with gadolinium rods in place are given in Fig. 46. The ratios of count rates with and without the poison were computed from the data in Figs. 24 and 46, and are shown in Fig. 47. No boron was present during any of the measurements with the poison rods.

2. **Small Assembly and Multiplication Effects.** PYTHON data from the 9×9 assembly with enriched and depleted pins are shown in Fig. 48; the ratios of the two counts are also given. The count rates are plotted in Fig. 49.

B. Gamma-Ray Measurements

PYTHON data with the ^{137}Cs gamma-ray source are shown in Figs. 50-51. The values are proportional to the current through the ionization chambers. An additional amplification stage was used because the strength of the source was much less than an actual spent-fuel assembly.

An exponential curve is shown fitted to the data points in Fig. 51. The linear attenuation coefficient for this curve is 0.1632 cm^{-1} , which is again between the values for water and UO_2 (at 662 keV) but closer to the value for water than the value with the fork. Gamma rays do indeed have to pass through more water to reach the PYTHON detector than they do the fork, so this attenuation coefficient is plausible.

The ionization chambers have a collimated field of view and raising the source even 5 cm out of the plane of the chambers reduced the signal to the background level. No gamma-ray axial profiles are thus presented for this detector.

	1	2	3	4	5	6	7	8	9
A			21.890		20.810		19.715		18.905
B	26.440								
C		26.610		24.940				23.170	
D									
E	30.890		26.555		27.505		26.850		25.865
F									
G		31.840		29.780		28.835		28.175	
H									
I	33.745				29.865		29.775		
J									
K		32.230		29.975		29.750		29.110	
L									
M	32.065		26.170		27.850		27.480		27.605
N									
O		26.735		25.335				24.820	
P	26.300								
Q			20.810		21.255		21.165		21.370

Fig. 35. PYTHON neutron data corresponding to the fork data in Fig. 8 are given in this figure. The 17×17 assembly contained 3.5%-enriched fuel. No boron was in the water.

	1	2	3	4	5	6	7	8	9
A			13.865		12.360		11.890		11.705
B 17.925									
C		17.400		15.430				14.255	
D									
E 21.715			18.545		16.960		16.350		16.050
F									
G		21.450		19.150		17.795		17.300	
H									
I 24.960					18.970		17.990		
J									
K		22.710		19.650		18.485		17.560	
L									
M 23.325			19.610		17.785		17.555		16.475
N									
O		19.585		16.970				14.790	
P 20.370									
Q			15.540		13.890		12.775		12.645

Fig. 36. These are PYTHON neutron count rates from the 17 x 17 array and 520 ppm boron in the water, corresponding to the fork data in Fig. 9.

	1	2	3	4	5	6	7	8	9
A			11.770		10.460		9.4000		9.1900
B 16.105									
C		15.535		12.935				11.035	
D									
E 19.315			16.005		13.815		12.825		13.060
F									
G		18.710		16.210		14.420		13.355	
H									
I 21.860					14.865		14.340		
J									
K		19.390		16.275		14.835		13.860	
L									
M 21.085			16.945		14.535		13.380		12.715
N									
O		17.250		13.945				11.690	
P 18.385									
Q			13.365		11.385		10.220		9.6150

Fig. 37. These are PYTHON neutron count rates from the 17 x 17 array and 1085 ppm boron in the water, corresponding to the fork data in Fig 10.

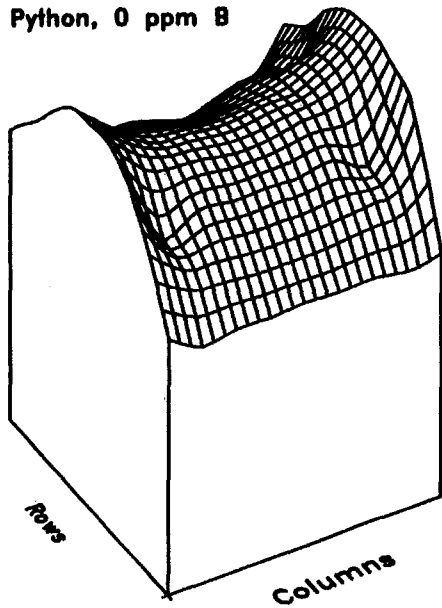
	1	2	3	4	5	6	7	8	9
A			10.020		8.3550		7.4400		7.0700
B	14.250								
C		13.385		10.620				8.4750	
D									
E	16.940		13.350		11.275		9.8300		9.4900
F									
G		16.160		13.030		11.355		10.405	
H									
I	19.045				11.760		10.985		
J									
K		16.985		13.625		11.445		10.430	
L									
M	18.800		14.125		11.720		10.205		9.9100
N									
O		15.030		11.225				8.9650	
P	16.680								
Q			11.550		9.1650		8.0050		7.4450

Fig. 38. These are PYTHON neutron count rates from the 17 x 17 array and 2170 ppm boron in the water, corresponding to the fork data in Fig 11.

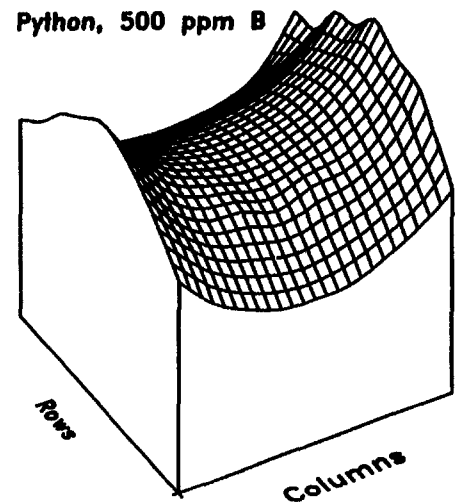
	1	2	3	4	5	6	7	8	9
A			9.1550		7.3550		6.4300		6.1500
B	13.460								
C		12.255		9.4200				7.4900	
D									
E	16.435		12.300		9.7600		8.6200		8.1950
F									
G		13.490		11.595		9.7050		8.8200	
H									
I	18.285				10.240		9.6750		
J									
K		15.350		11.800		10.025		9.2550	
L									
M	17.740		13.050		10.415		8.9100		8.6800
N									
O		14.185		10.615				7.8900	
P	15.505								
Q			10.565		8.3050		7.0550		6.5950

Fig. 39. These are PYTHON neutron count rates from the 17 x 17 array and 2829 ppm boron in the water, corresponding to the fork data in Fig 12.

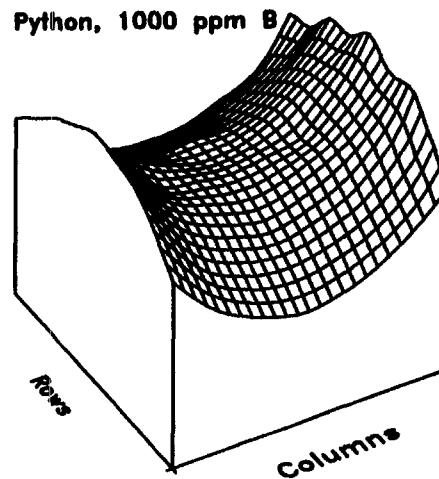
Python, 0 ppm B



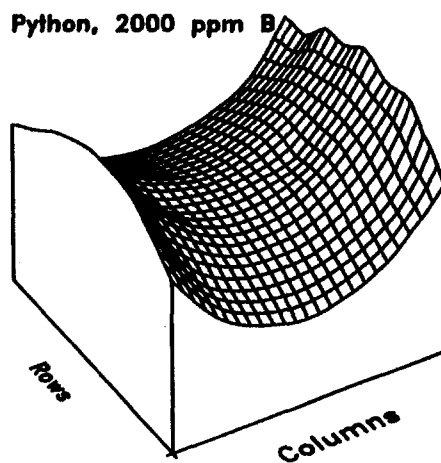
Python, 500 ppm B



Python, 1000 ppm B



Python, 2000 ppm B



Python, 3000 ppm B

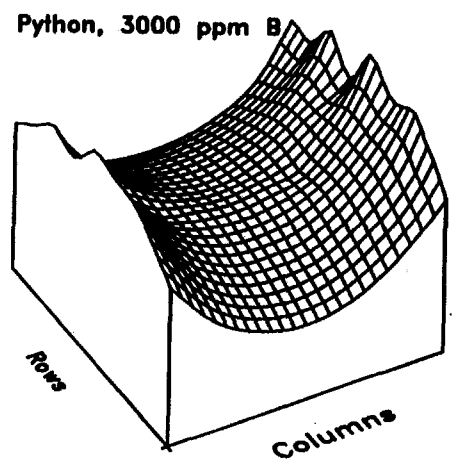


Fig. 40. The count rates from PYTHON fission chambers (Figs. 35-39) are shown graphically. The scales of the diagrams are all the same, so the effects of different boron concentrations can be seen qualitatively. Count rates for columns 10-17 were set equal to those from columns 8-1, respectively. The ripples along the borders are artifacts of the interpolation process used in generating the diagrams.

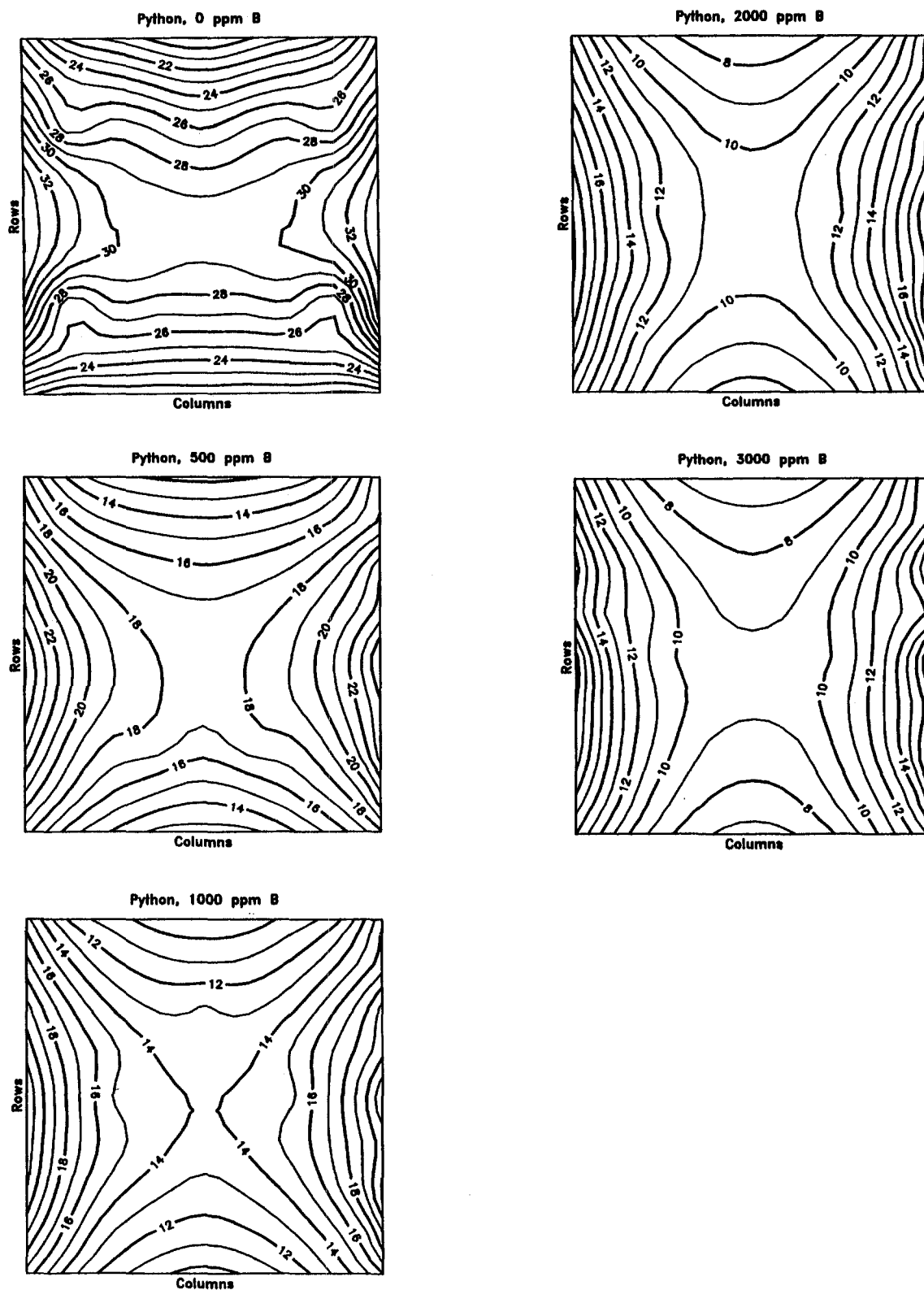
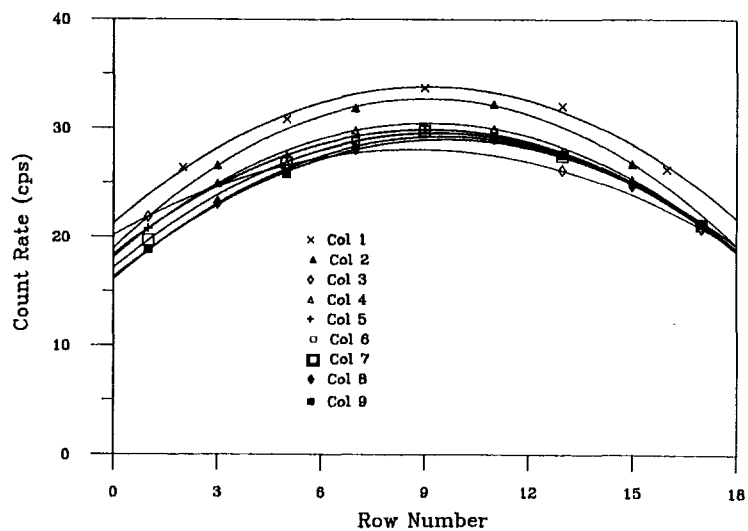
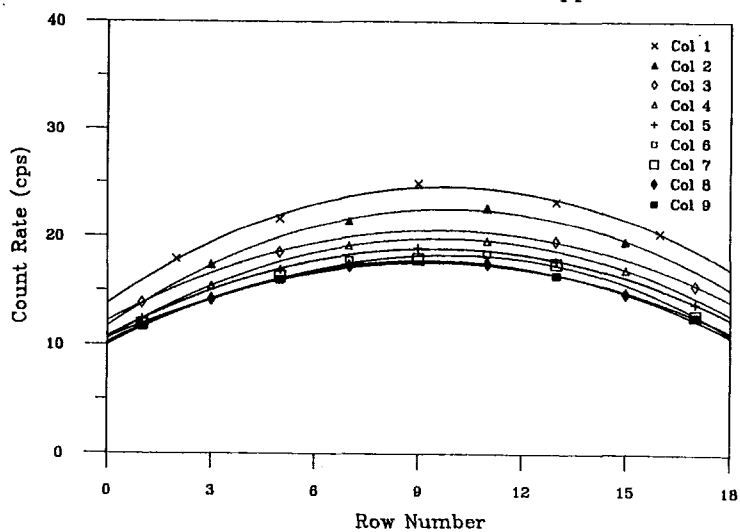


Fig. 41. The data from PYTHON fission chambers (Figs. 35-39) are used to generate contour plots of count rates at different boron concentrations. Count rates for columns 10-17 were set equal to those from columns 8-1, respectively.

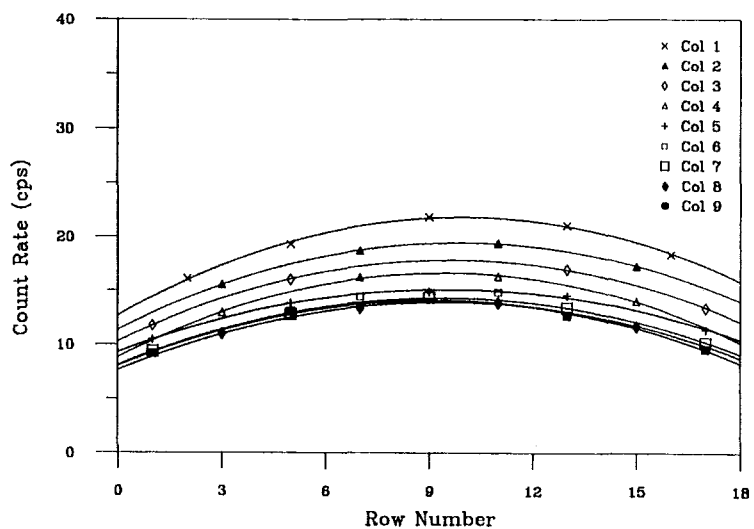
PYTHON Column Profiles, 0 ppm B



PYTHON Column Profiles, 500 ppm B



PYTHON Column Profiles, 1000 ppm B



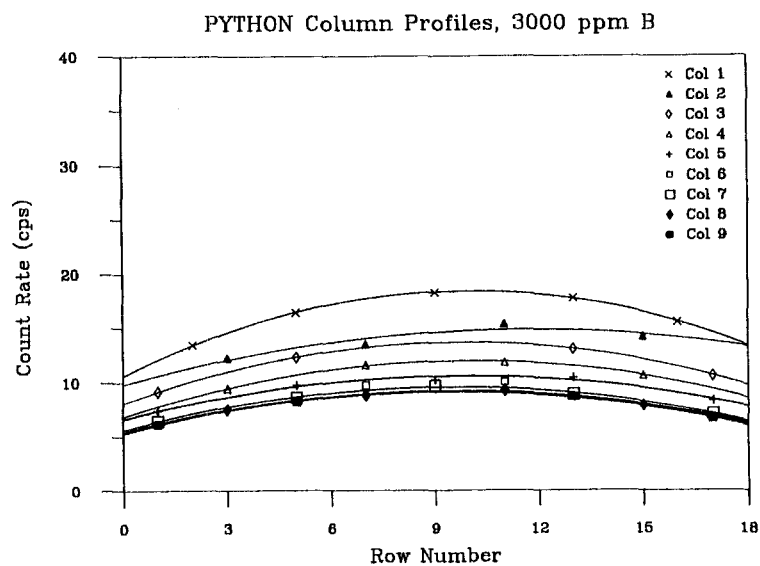
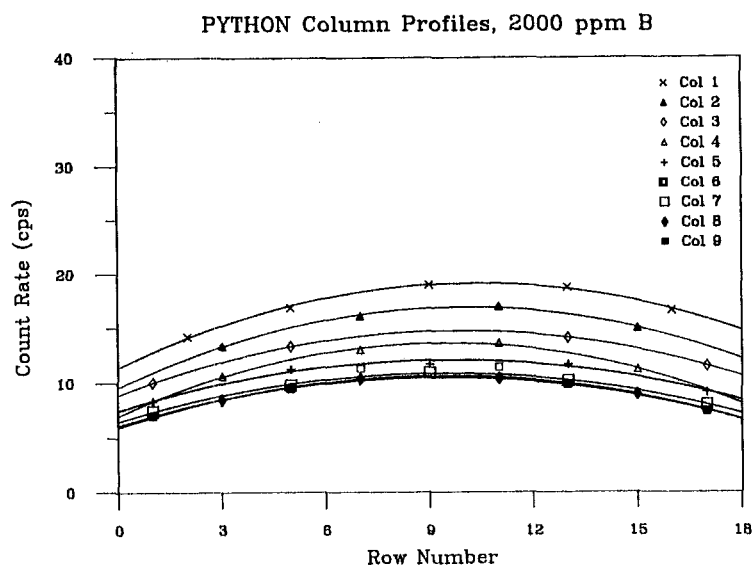
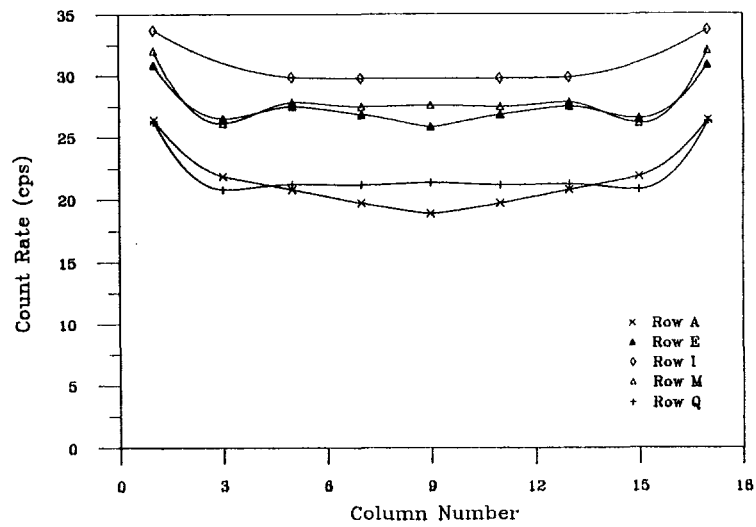
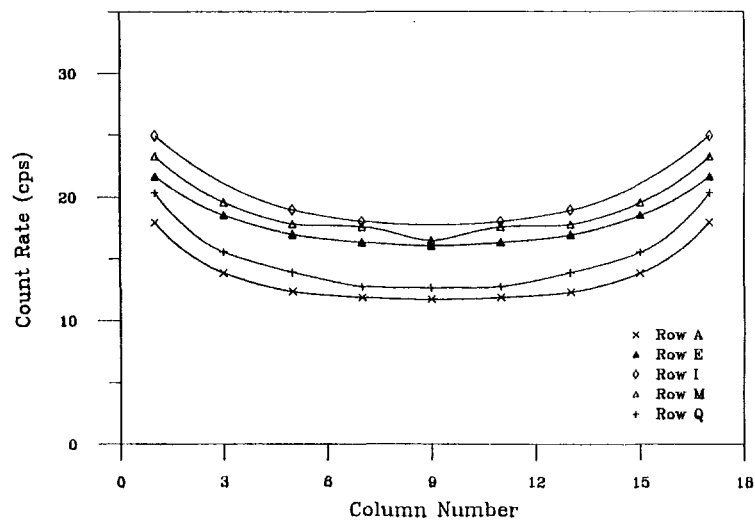


Fig. 42. The PYTHON neutron data of Figs. 35-39 are shown graphically by connecting the data from pins in the same column; the curves have no significance beyond helping the viewer organize the data. Columns nearest the fork's tines produced the highest count rates.

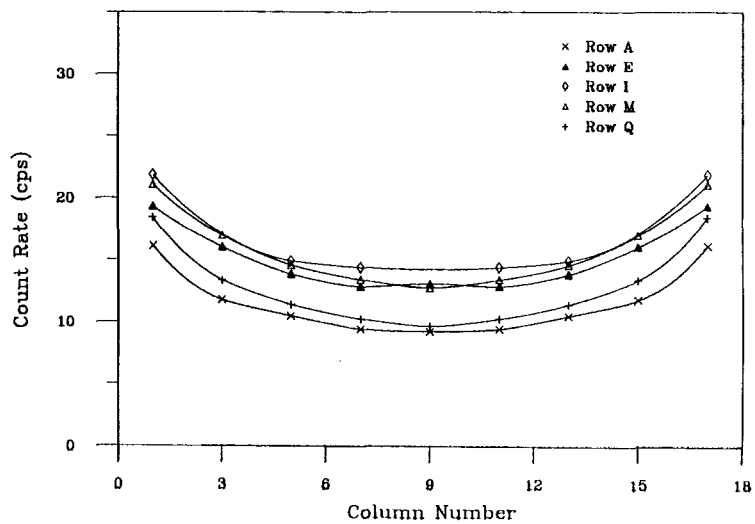
PYTHON Row Profiles, 0 ppm B



PYTHON Row Profiles, 500 ppm B



PYTHON Row Profiles, 1000 ppm B



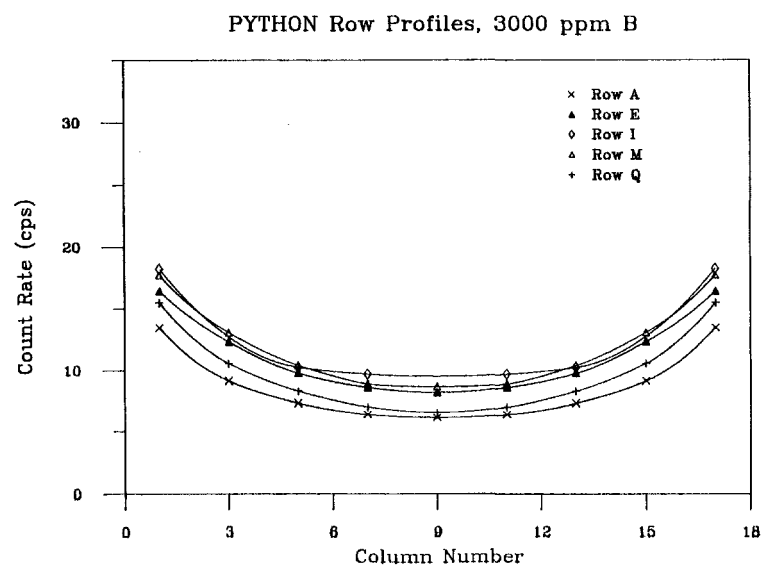
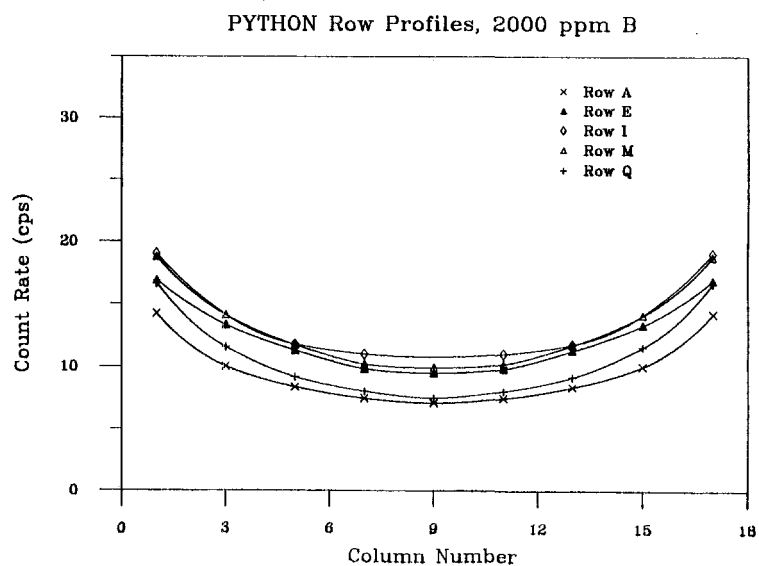
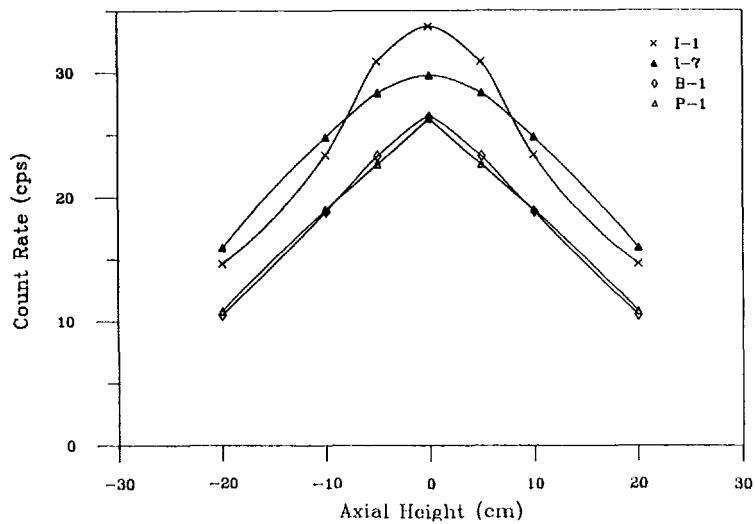
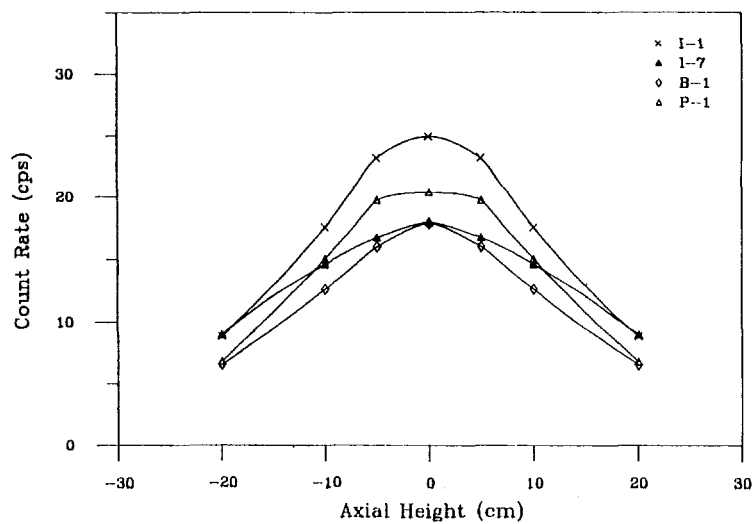


Fig. 43. The caption to Fig. 42 applies here, except that data from the same rows are shown connected by curves.

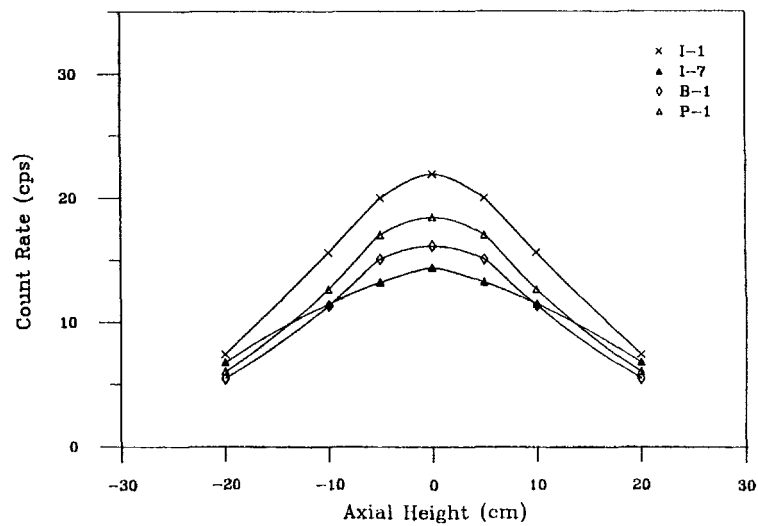
PYTHON Axial Profiles, 0 ppm B



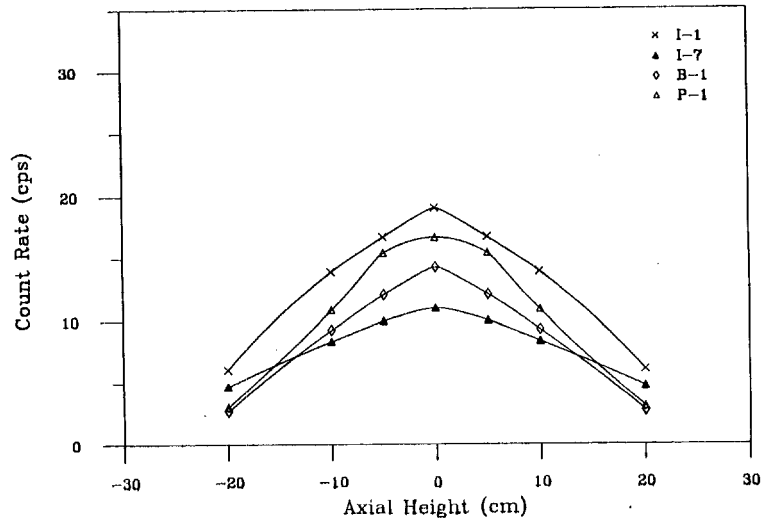
PYTHON Axial Profiles, 500 ppm B



PYTHON Axial Profiles, 1000 ppm B



PYTHON Axial Profiles, 2000 ppm B



PYTHON Axial Profiles, 3000 ppm B

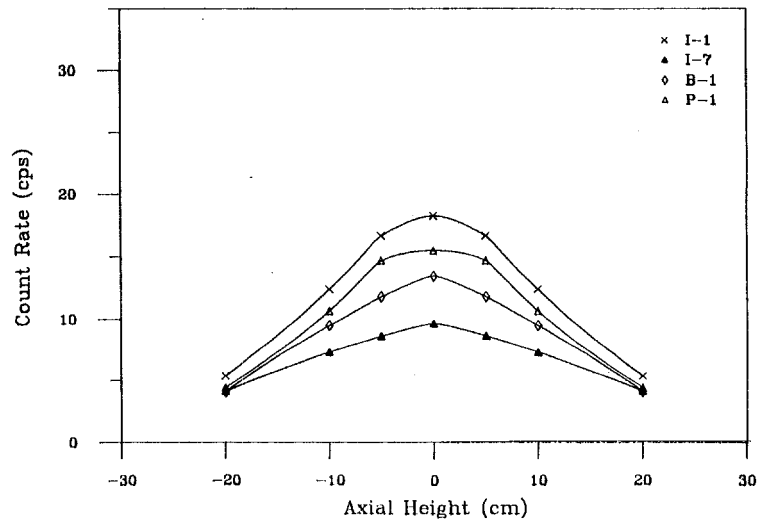


Fig. 44. The PYTHON neutron axial profile data from Tables X-XIV are shown here graphically. Data were taken at only positive vertical displacements, but the same data were used at negative displacements to generate these symmetric profiles.

TABLE X. Axial PYTHON Neutron Data at 0 ppm Boron

Vertical Distance (cm)	Counts per Second				
	I-1	I-5	I-7	B-1	P-1
0	33.75 ± 1.86	29.87 ± 0.82	29.78 ± 0.81	26.44 ± 0.98	26.30 ± 1.05
5	30.88 ± 0.84	-----	28.38 ± 0.92	23.32 ± 0.89	22.63 ± 0.86
10	23.41 ± 0.80	-----	24.83 ± 0.72	18.86 ± 0.62	19.00 ± 0.84
20	14.62 ± 0.56	-----	15.96 ± 0.58	10.48 ± 0.53	10.80 ± 0.53

TABLE XI. Axial PYTHON Neutron Data at 520 ppm Boron

Vertical Distance (cm)	Counts per Second				
	I-1	I-5	I-7	B-1	P-1
0	24.96 ± 1.18	18.97 ± 0.78	17.99 ± 0.66	17.93 ± 0.77	20.37 ± 0.97
5	23.20 ± 1.12	17.70 ± 0.59	16.76 ± 0.73	16.00 ± 0.72	19.72 ± 1.37
10	17.60 ± 0.86	14.95 ± 0.69	14.62 ± 0.50	12.59 ± 0.79	15.04 ± 0.96
20	8.86 ± 0.59	9.00 ± 0.48	8.99 ± 0.38	6.58 ± 0.45	6.84 ± 0.45

TABLE XII. Axial PYTHON Neutron Data at 1085 ppm Boron

Vertical Distance (cm)	Counts per Second				
	I-1	I-5	I-7	B-1	P-1
0	21.86 ± 1.15	14.87 ± 0.72	14.34 ± 0.62	16.11 ± 0.99	18.39 ± 1.00
5	19.98 ± 0.90	14.26 ± 0.56	13.20 ± 0.48	15.03 ± 0.68	16.98 ± 0.89
10	15.58 ± 0.71	11.99 ± 0.58	11.45 ± 0.56	11.31 ± 0.69	12.62 ± 1.03
20	7.40 ± 0.48	6.80 ± 0.44	6.74 ± 0.47	5.43 ± 0.35	5.97 ± 0.50

TABLE XIII. Axial PYTHON Neutron Data at 2170 ppm Boron

Vertical Distance (cm)	Counts per Second				
	I-1	I-5	I-7	B-1	P-1
0	19.05 ± 1.40	11.76 ± 0.55	10.99 ± 0.62	14.25 ± 1.00	16.68 ± 1.38
5	16.69 ± 0.77	11.00 ± 0.55	9.99 ± 0.54	12.10 ± 1.02	15.43 ± 1.34
10	13.89 ± 0.89	9.11 ± 0.43	8.32 ± 0.39	9.23 ± 0.78	10.84 ± 0.84
20	6.04 ± 0.57	5.02 ± 0.41	4.70 ± 0.35	2.73 ± 0.27	3.08 ± 0.44

TABLE XIV. Axial PYTHON Neutron Data at 2829 ppm Boron

Vertical Distance (cm)	Counts per Second				
	I-1	I-5	I-7	B-1	P-1
0	18.29 ± 1.50	10.24 ± 0.61	9.68 ± 0.50	13.46 ± 1.15	15.51 ± 1.29
5	16.63 ± 1.11	9.77 ± 0.49	8.66 ± 0.53	11.80 ± 0.99	14.71 ± 1.22
10	12.39 ± 0.98	8.06 ± 0.43	7.30 ± 0.45	9.50 ± 1.11	10.68 ± 0.79
20	5.38 ± 0.42	4.42 ± 0.39	4.17 ± 0.28	4.14 ± 0.40	4.47 ± 0.48

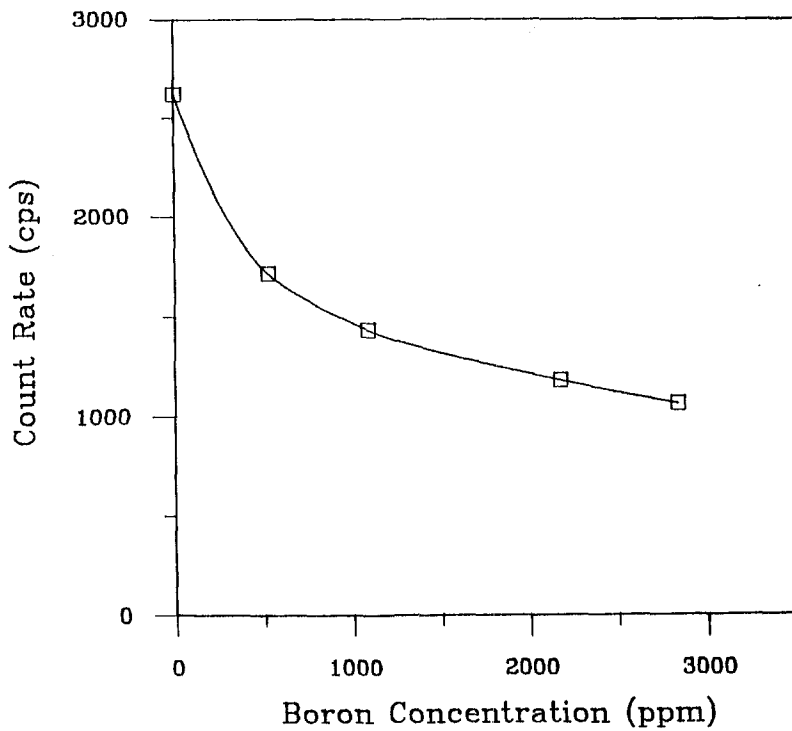


Fig. 45. Sums of PYTHON count rates from Figs. 35-39 are displayed graphically and given numerically in Table VII. The unmeasured count rates expected from columns 10-17 are taken equal to the count rates in columns 1-8.

	1	2	3	4	5	6	7	8	9
A									
B									
C									
D									
E			17.850		15.710				
F									
G									
H									
I	23.085				17.725		16.960		
J									
K									
L									
M			18.865		16.580				
N									
O									
P									
Q									

Fig. 46. The PYTHON neutron count rates from seven pin locations are shown with gadolinium poison rods inside the array. The poison rods are at the 15 locations of Fig. 7 shown as solid black circles in columns 3, 4, 6, and 9.

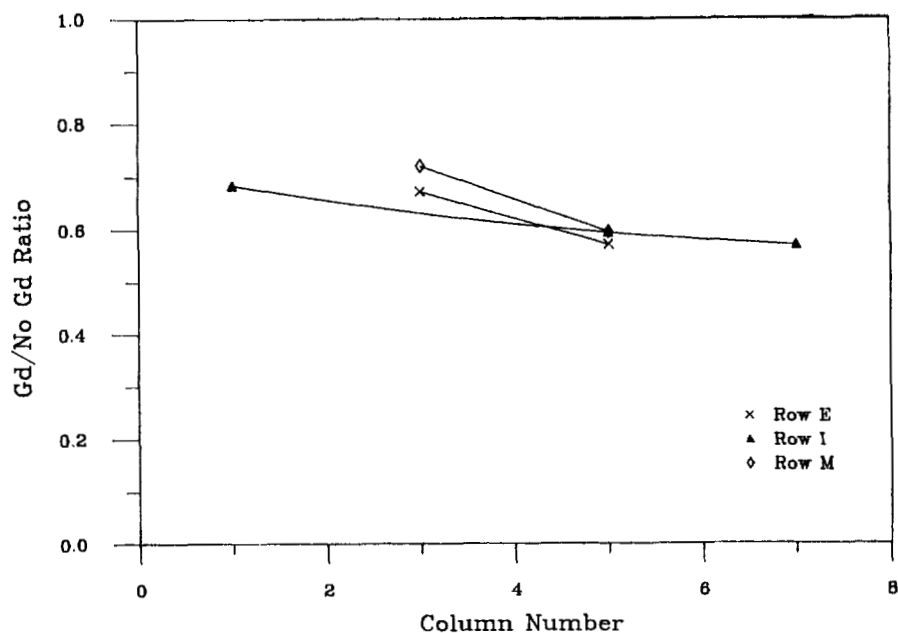


Fig. 47. Ratios of PYTHON count rates without and with gadolinium poison rods present are shown. These ratios decrease slowly as the source moves more to the interior of the assembly. No boron was present during these measurements.

0.25%
3.50%
0.25/3.50

	1	2	3	4	5	6	7	8	9
A									
B									
C									
D					5.3950 11.090 .48647				
E	13.070 18.420 .70955	10.370 16.195 .64032	8.4250 13.955 .60373	6.7050 12.350 .54291	5.6600 11.050 .51222	4.7500 9.9450 .47763	4.1350 9.0800 .45540	3.6700 8.4300 .43535	3.5000 7.5550 .46327
F					5.6100 11.025 .50884				
G									

Fig. 48. Neutron count rates with the 9 x 9 array of Fig. 26 and the PYTHON detector are shown here. At each source location three numbers are shown; from top to bottom they are the count rate with depleted uranium pins, the count rate with 3.5%-enriched uranium pins, and the ratio of the depleted count rate to the enriched count rate. The source was placed in each position of row H that goes through the middle of the array.

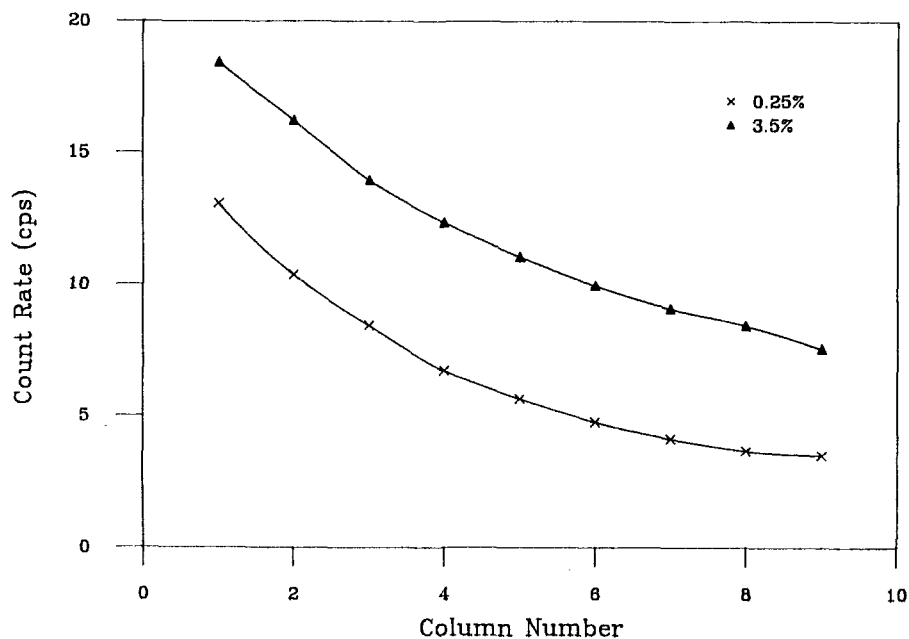


Fig. 49. The PYTHON data of Fig. 48 are shown graphically. The multiplication effect is from the higher count rates with the enriched fuel.

	1	2	3	4	5	6	7	8	9
A		18.500							
B	27.290								
C	31.480	19.090							
D									
E	31.440	19.200							
F									
G	32.050	24.280	19.630	16.980	14.630				
H									
I	36.900	18.330							
J									
K	36.120	21.880							
L									
M	35.750	21.500							
N									
O	34.000	21.100							
P	27.510								
Q		22.000							

Fig. 50. These PYTHON gamma-ray data are the voltages corresponding to the ionization chamber currents from a ^{137}Cs source at the locations indicated by the presence of the data. Uncertainties (1σ) are generally about 0.15 V.

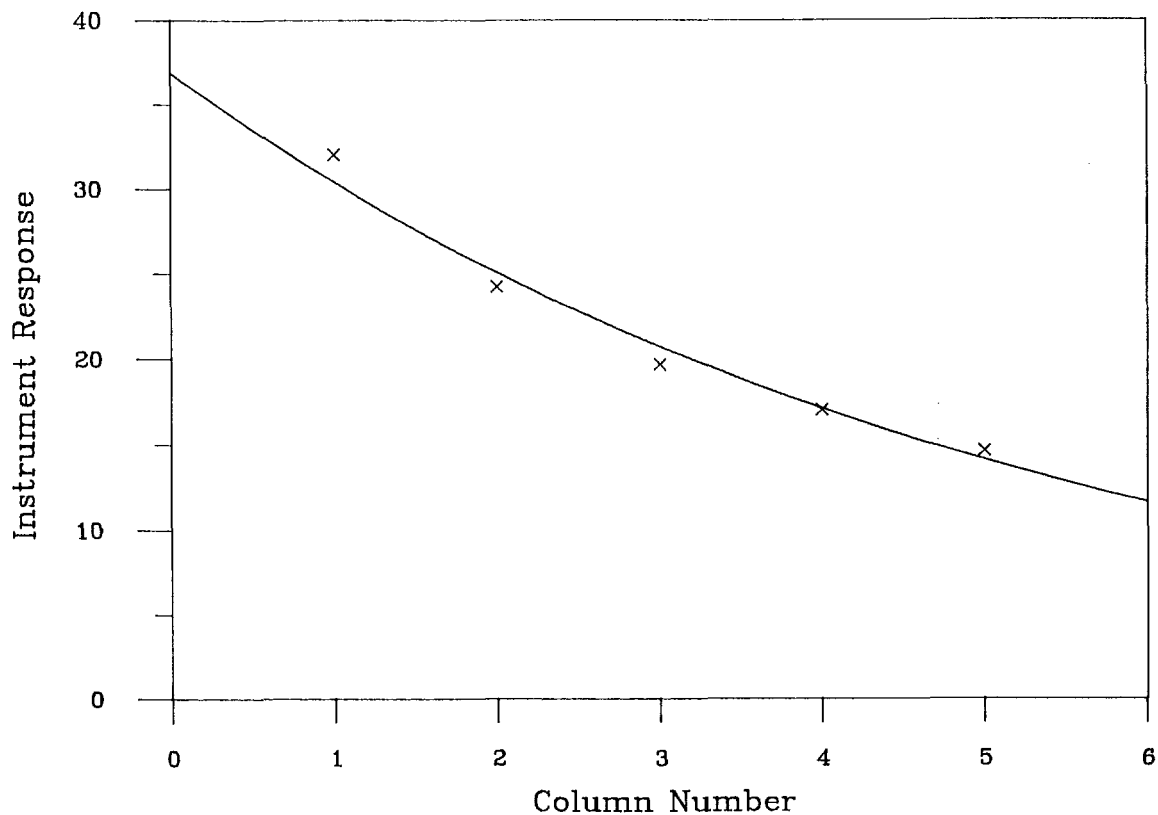


Fig. 51. The PYTHON gamma-ray data of Fig. 50 are shown graphically. The curves connect data from pins in row G (see Fig. 7). An exponential curve is shown fitted to the data; its exponent is 0.1632 cm^{-1} .

V. FORK AND PYTHON COMPARISONS

A. Neutron Measurements

1. Standard Assembly

a. **Source Position Sensitivities.** From pairs of figures, such as Figs. 8 and 35, the responses of the fork and PYTHON detectors to neutrons throughout an assembly can be compared. Data from the cadmium-wrapped fission chambers should correlate more closely with the PYTHON data than do the fork's bare fission chamber data because of the neutron absorbers surrounding the PYTHON neutron detectors.

Three immediately obvious observations from the figures are that (a) the fork detector generates higher count rates, (b) the profiles from PYTHON are flatter, and (c) the fork's axial neutron profiles are more narrow than PYTHON's.

The fork count rates (Figs. 8-12) are consistently higher than PYTHON's (Figs. 35-39). Although the fork's fission chambers are relatively small, they are placed closer to the assembly.

Ratios of fork and PYTHON count rates along various rows and columns are shown in Figs. 52-53. These ratios are in the vicinity of 3.5, but the relative flatness of the PYTHON column profiles leads to arched curves in Fig. 52. The greater length of the PYTHON detectors is an advantage, particularly for safeguards measurements where diversion of a pin from any position is important. The shapes of the two sets of row profiles are more similar than the sets of column profiles, so the curves in Fig. 53 are more nearly flat. The fork's greater sensitivity to pins near the tines generally produces some upturn of the curves at the edges of the assembly.

The axial profiles of Figs. 21 and 44 show that when the neutron source was raised out of the detectors' planes, the count rate from the fork fell by half after a displacement of about 10 cm while the same fractional decrease took about 20 cm for PYTHON. The differences in the physical sizes of the fission chambers and their positions relative to the assembly account for these behaviors. The more narrow axial view of the fork is an advantage in safeguards examinations, but not necessarily in criticality safety measurements.

b. Total Count Rates. Sums of individual pin count rates are shown in Figs. 23 and 45. The count rates in columns 1-8 were doubled to account for the unmeasured contributions from columns 10-17. PYTHON has a greater range along the assembly's axis than the fork, so the planar data from PYTHON were multiplied by 1.4 to allow a more direct comparison between the two detectors' results. Although this factor actually varies with the source's position and the boron concentration, the value 1.4 is a good representative value for the whole assembly and all concentrations.

The last column in Table VII shows that the fork generates about three times PYTHON's count rate. The count rate from PYTHON with actual spent-fuel assemblies is still high enough to gather the necessary number of counts in a short time, even from an assembly in motion (Fig. 5).

These sums are from pin locations distributed uniformly throughout the assembly and thus are expected to be proportional to count rates from actual spent-fuel assemblies. The sum from a similar subset of 34 pin locations for a 15×15 array³ was found to be proportional to the sum from all 204 pins regardless of boron concentration. The proportionality factor was simply the ratio of the numbers of pins ($204/34 = 6$). In this case, the expected count rates from the source located in all pin

locations are thus $265/70 = 3.786$ times the sum of count rates in Table VII and Figs. 23 and 45.

c. **Gadolinium Poison Effects.** The gadolinium poison rods had about the same effects on the two detectors' responses (Figs. 25 and 47).

The similarity of the fork curves in Fig. 25 for cadmium-wrapped and bare fission chambers shows that the poison affects the apparent neutron source strength and not the spectrum of the neutrons escaping the assembly. If the gadolinium preferentially reduced the number of escaping thermal neutrons, the bare detector's count rate would have dropped by a larger fraction than the cadmium-wrapped detector's count rate.

2. **Small Assembly and Multiplication Effects.** The profiles shown in Figs. 29 and 49 from the 9×9 pin array are quite similar, aside from the slightly higher fork count rates from columns 1 and 2. These data from unusually small arrays are useful for benchmarking computer transport codes.

B. Gamma-Ray Measurements: Source Position Sensitivities

Both detectors found that the exponential attenuation expression works quite well for the transport of 662-keV gamma rays through an assembly underwater. The attenuation coefficient depends on the amount of water between the assembly and the detector and thus differs for the two detectors.

The relative importances of pins in various columns are now known by direct measurement. With these data a rather simple gamma-ray transport calculation can be done instead of a Monte Carlo calculation.

C. Correlation Summary

From the data in this report, correlations between detector responses can be made. The neutron and gamma-ray values were measured with both detectors under the same conditions, and integrated responses have been estimated.

1. **Neutrons.** The correlation of the fork and PYTHON neutron responses is found from Table VII. The ratios of sums in the last column show that there is a dependence on boron concentration, but concentrations in plants are either zero or

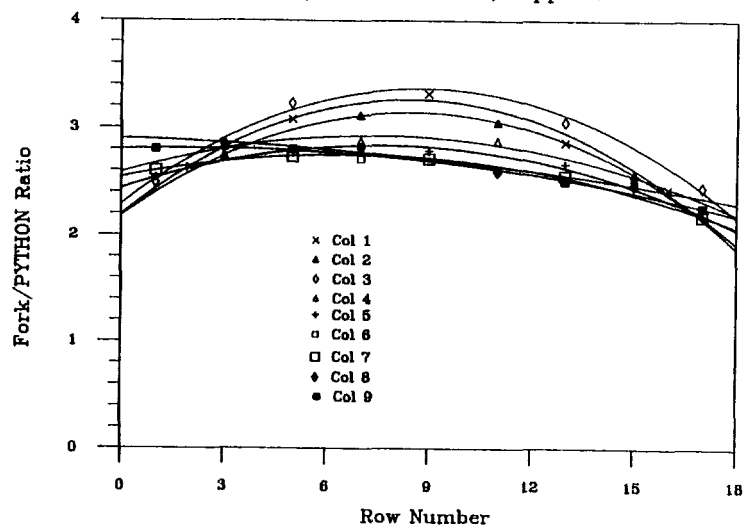
between 2000 and 3000 ppm. If a spent-fuel assembly was measured with PYTHON, it is expected that the fork's count rate from the cadmium-wrapped fission chambers would be 2.74 or 3.16 times larger, respectively.

This correlation has been found for a 17 x 17 PWR assembly without poison or control rods present and with 3.5%-enriched fuel pins. A spent-fuel assembly would have a smaller enrichment in the remaining fuel, so the multiplication will be reduced. The count rates are proportional to the multiplication, $1/(1 - k_{\text{eff}})$, so the ratio of the two detectors' responses is unchanged. The above correlation factors should still be valid.

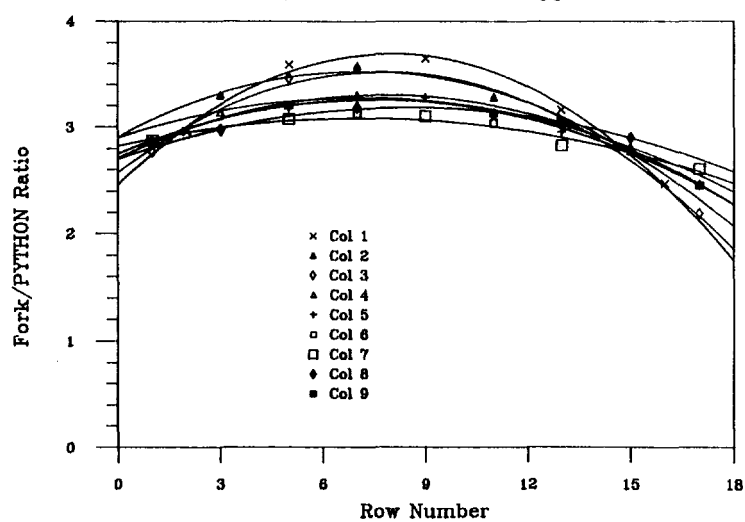
2. Gamma Rays. The correlation between gamma-ray detectors can not be well established for two reasons. First, an extra amplifier was attached to PYTHON to get usable signals from the weak ^{137}Cs source. Second, there was insufficient time to map gamma-ray responses over a representative set of pin positions; it was judged more important to concentrate on the neutron measurements.

However, from the data on hand (Figs. 32 and 50), with the increased PYTHON signal, the ratio of fork-to-PYTHON summed responses is 0.000326. This correlation should not be used without carefully considering the measurement circumstances. The PYTHON gamma-ray values vary much more slowly with position than do those from the fork.

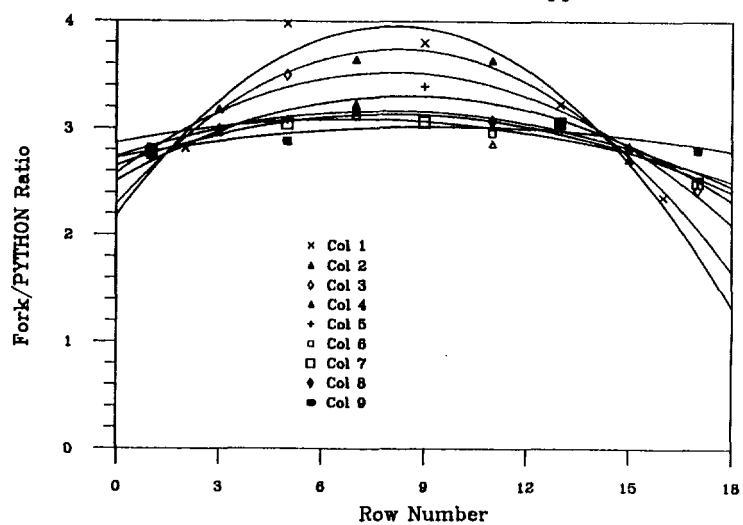
Fork/PYTHON Ratios, 0 ppm B



Fork/PYTHON Ratios, 500 ppm B



Fork/PYTHON Ratios, 1000 ppm B



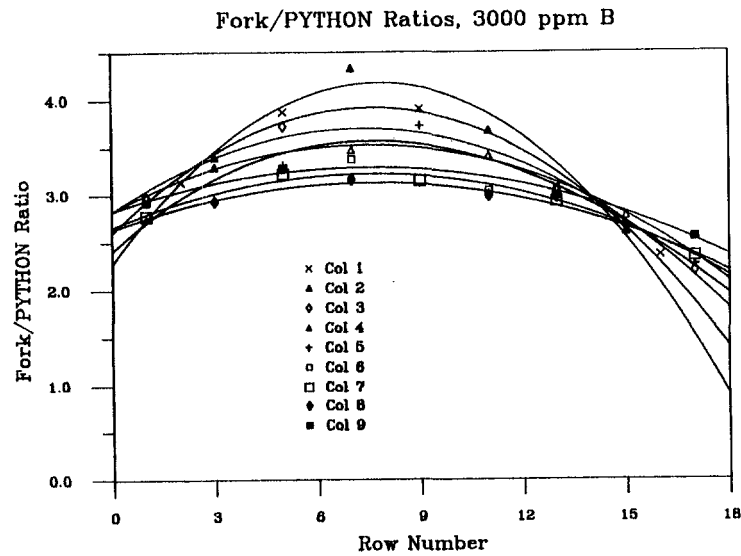
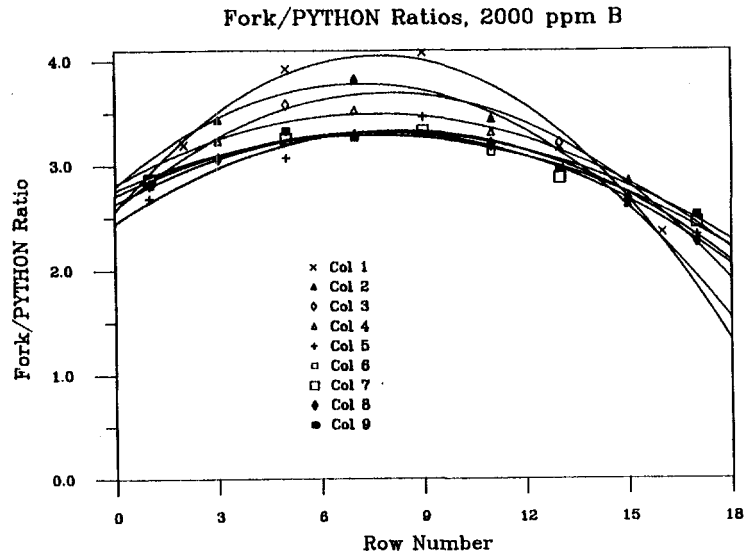
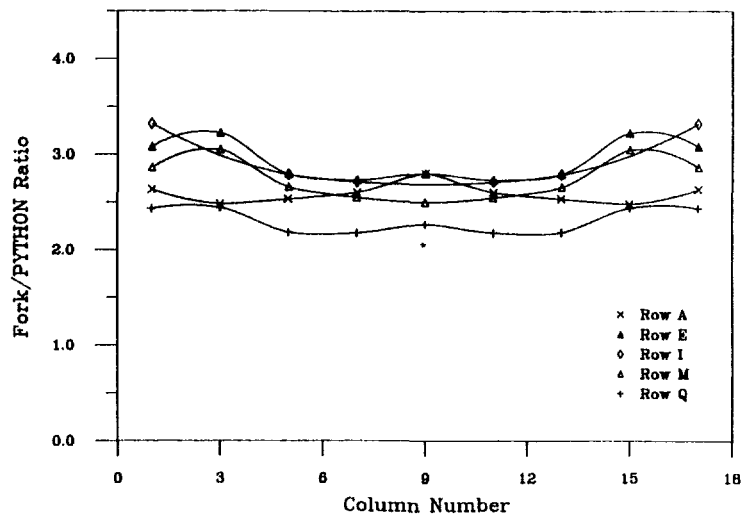
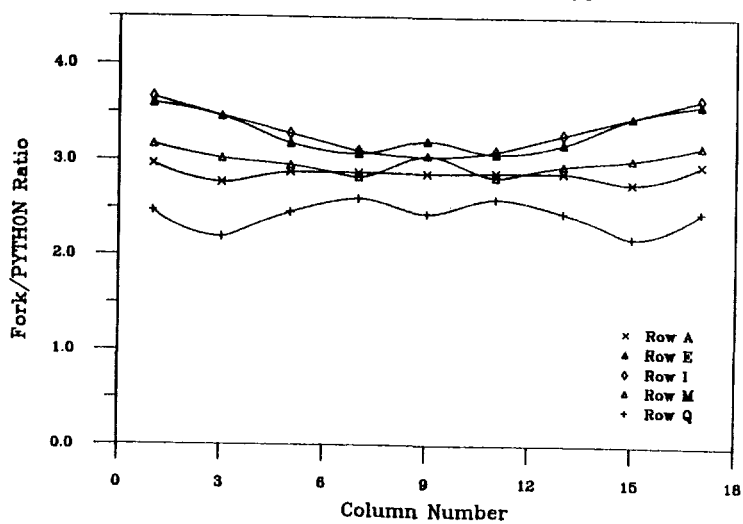


Fig. 52. Ratios of fork and PYTHON neutron count rates are shown here with data from each column (see Fig. 7) connected by a smooth curve. These are ratios of the data in Figs. 8-12 (cadmium) and 35-39 with different concentrations of boron in the water. Column 1 is nearest the detectors and column 9 is midway between the detectors' sections. The pronounced arching from the first three columns is a result of the shorter fission chambers used in the fork; the fork's count rates from positions near the assembly's corners are reduced because of the distance to the fission chambers.

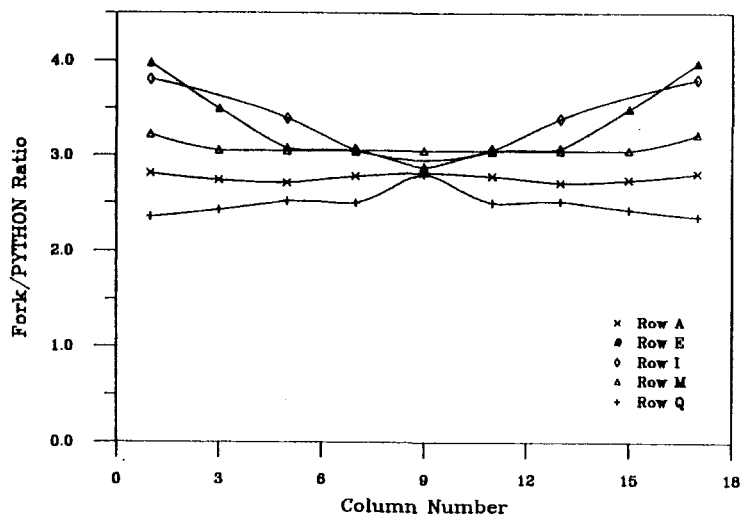
Fork/PYTHON Row Ratios, 0 ppm B



Fork/PYTHON Row Ratios, 500 ppm B



Fork/PYTHON Row Ratios, 1000 ppm B



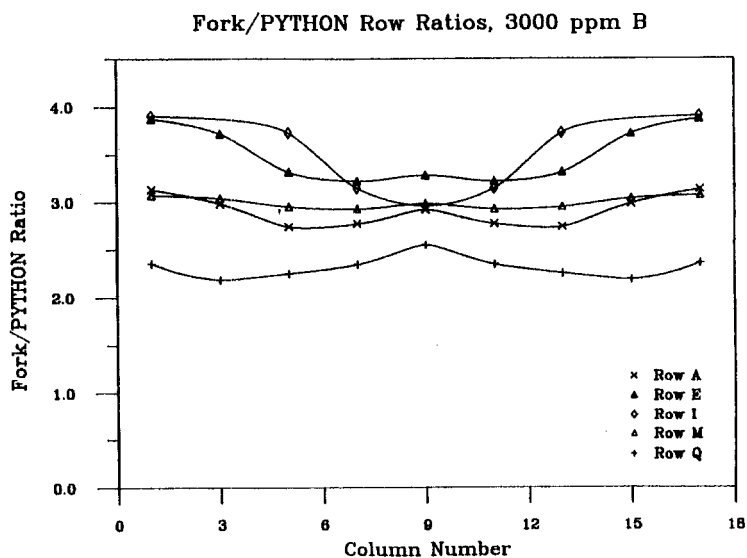
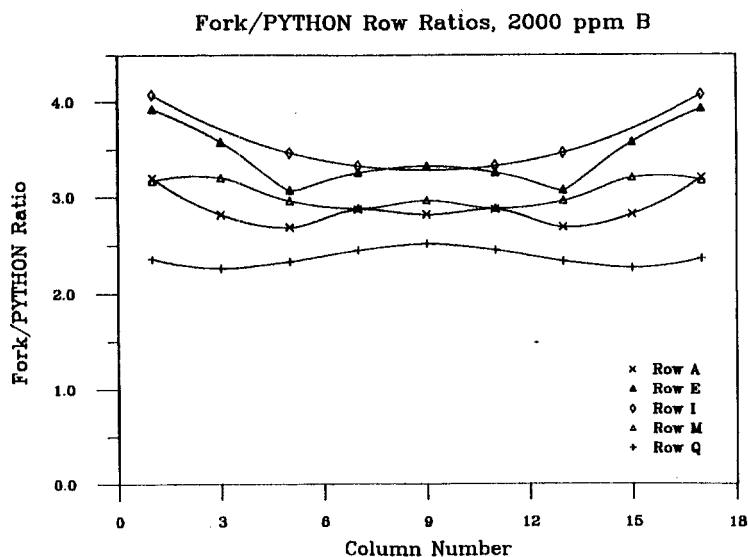


Fig. 53. Ratios of fork and PYTHON neutron count rates are shown here with data from each row (see Fig. 7) connected by a smooth curve. These are ratios of the data in Figs. 8-12 (cadmium) and 35-39 with different concentrations of boron in the water. Rows A and Q are edges of the assembly and Row I is through the middle of the assembly. The slight tendency for the curves to rise near the detectors (columns 1 and 17) is a result of the fork's nearness to the assembly and enhanced sensitivity to the nearest columns of pins.

VI. SUMMARY

A. Objectives and Instrument Features

The developments of spent-fuel detectors by the United States and France have taken different paths because of different objectives and measurement conditions. The design of an instrument has been affected by whether it is to be used for safety purposes in a friendly environment or for safeguards purposes in a potentially uncooperative atmosphere.

The United States has had to consider transportability (across international boundaries) and rapid measurements with only partial movement of the fuel from the rack; these have led to a small, lightweight instrument with a battery-powered electronics unit for use on a pond's bridge.

For domestic use in France the larger instrument can remain fixed in a storage pond and fuel brought to it. The electronics has standard components and can run from a building's main supply. The capability of active measurements with a ^{252}Cf source is a powerful feature because it can measure the fissile material directly instead of measuring an isotope such as ^{244}Cm that is correlated with the fissile content.

B. Responses and Correlations

The larger, more distant neutron and gamma-ray detectors in PYTHON generate more uniform responses to pins throughout an assembly, compared with the fork detector. This larger geometry causes lower neutron count rates and gamma-ray signals, but with the high emission rates from spent-fuel assemblies this is not a problem.

From the neutron measurements, a correlation between neutron count rates is established. For water without boron, the fork count rate is 2.74 times PYTHON's. Boronated water usually has between 2000 and 3000 ppm boron, and the multiplier in this case is 3.16. Information in this report can be used for lower concentrations, should they be encountered.

A correlation between gamma-ray responses is not so well known because PYTHON required an additional amplifier stage with the weak source used and data were not taken throughout as much of the assembly as in the neutron case. However, the gamma-ray data are very valuable in giving a direct measurement of the relative importances of the pins at different distances from the detectors. Pins farther inside assemblies' interiors than those used in past calculation should be considered.

VII. ACKNOWLEDGMENTS

Leo Cowder of Los Alamos assisted with the preparations of the fork detector and Guy Coquillat helped with the measurements. The hospitality of the Cadarache personnel is impossible to match and is greatly appreciated by those from the United States.

REFERENCES

1. P. M. Rinard and G. E. Bosler, "BWR Spent Fuel Measurements with the ION-1/Fork Detector and a Calorimeter," Los Alamos National Laboratory report LA-10758-MS (August 1986).
2. P. M. Rinard and G. E. Bosler, "Safeguarding LWR Spent Fuel with the Fork Detector," Los Alamos National Laboratory report LA-11096-MS (March 1988).
3. P. M. Rinard, "Neutron Measurements in Borated Water for PWR Fuel Inspections," Los Alamos National Laboratory report LA-10068-MS (July 1984).
4. J. R. Phillips, G. E. Bosler, J. K. Halbig, S. F. Klosterbuer, and H. O. Menlove, "Nondestructive Verification with Minimal Movement of Irradiated Light-Water Reactor Fuel Assemblies," Los Alamos National Laboratory report LA-9438-MS (October 1982).
5. G. E. Bosler, P. M. Rinard, S. F. Klosterbuer, and J. Painter, "Automated Methods for Real-Time Analysis of Spent-Fuel Measurement Data," in *Proc. 29th Annual Meeting of the Institute of Nuclear Materials Management XVII*, June 26-29, 1988, Las Vegas, Nevada, pp. 487-493.
6. P. Bernard, R. Berne, R. Bosser, J. Cloue, A. Giacometti, A. le Person, J. Pinel, and J. Romeyer-Dherbey, "Active and Passive NDA Methods for Nuclear Materials," *Proc. Third International Conference on Facility Operations--Safeguards Interface*, November 29-December 4, 1987, San Diego, California (American Nuclear Society, La Grange Park, Illinois, USA).
7. G. Bignan, J. Capsie, P. M. Rinard, and J. Romeyer-Dherbey, "Intercomparaison des Dispositifs Python (C.E.A.) et Ion-Fork (D.O.E.) pour le Controle des Assemblages Irradies," Commissariat a l'Energie Atomique report, Note Technique SSAE/LDMN/89-037 (1989).

8. N. Ensslin, J. Stewart, and J. Sapir, "Self Multiplication Correction Factors for Neutron Coincidence Counting," *J. Inst. Nucl. Mater. Manage.* VIII(2), pp. 60-73, Summer 1979.
9. P. M. Rinard, "Gamma Doses from Irradiated Assemblies Under Water," Los Alamos Scientific Laboratory report LA-7914-MS (July 1979).
10. J. R. Phillips and G. E. Bosler, "Calculated Response Contributions of Gamma Rays Emitted from Fuel Pins in an Irradiated PWR Fuel Assembly," Los Alamos National Laboratory report LA-10068-MS (August 1983).

This report has been reproduced directly from
the best available copy.

Available to DOE and DOE contractors from
the Office of Scientific and Technical Information
P.O. Box 62
Oak Ridge, TN 37831
prices available from
(615) 576-8401, FTS 626-8401

Available to the public from
the National Technical Information Service
U.S. Department of Commerce
5285 Port Royal Rd.
Springfield, VA 22161

Microfiche A01

NTIS		NTIS		NTIS		NTIS	
Page Range	Price Code	Page Range	Price Code	Page Range	Price Code	Page Range	Price Code
001-025	A02	151-175	A08	301-325	A14	451-475	A20
026-050	A03	176-200	A09	326-350	A15	476-500	A21
051-075	A04	201-225	A10	351-375	A16	501-525	A22
076-100	A05	226-250	A11	376-400	A17	526-550	A23
101-125	A06	251-275	A12	401-425	A18	551-575	A24
126-150	A07	276-300	A13	426-450	A19	576-600	A25
						601-up*	A99

*Contact NTIS for a price quote.

